Visualization and analysis of magnetothermal convection of paramagnetic liquid in the Rayleigh-Benard model

Syou Maki,[1,*] Noriyuki Hirota,[2] and Masayuki Hagiwara[3]
[1]*Laboratory of Molecular Chemistry, Faculty of Pharmacy, Osaka Ohtani University, 3-11-1 Nishikiori-kita, Tondabayashi, Osaka Prefecture 584-8540, Japan*
[2]*Fine Particles Engineering Group, National Institute for Materials Science, 1-2-1 Sengen, Tsukuba, Ibaraki Prefecture 305-0047, Japan*
[3]*Center for Advanced High Magnetic Field Science (AHMF), Graduate School of Science, Osaka University, 1-1 Machikaneyama, Toyonaka, Osaka Prefecture 560-0043, Japan*

(Received 24 July 2017; revised manuscript received 20 December 2017; published 12 September 2018)

We examined the heat transfer of magnetothermal convection in a Rayleigh-Benard model (height 9.2 mm, vessel diameter 20 mm, aspect ratio 2.17). The working fluid was an aqueous gadolinium nitrate solution of 0.15 mol/kg (pH = 4.52 at 305.5 K, paramagnetic substance). Not only the magnetic body force but also the temperature dependence of paramagnetic susceptibility according to Curie's law provides the driving body force of convection and exerts a decisive influence over the heat transfer performance. The visual observation of the isothermal contour of convection was realized by the addition of a thermochromic liquid crystal (TLC). Using a large upward magnetic body force, i.e., $(\vec{b}\cdot\vec{\nabla})b_z = 83.31\ \mathrm{T^2/m}$ at the vessel center, we succeeded in visualizing the horizontal isothermal illuminant of the TLC, which revealed the realization of a quasiweightless condition in the Rayleigh-Benard model. The heat transfer on convection was analyzed by the method of Churchill and Ozoe. Its performance was enhanced by the downward magnetic body force and was suppressed by the upward magnetic body force, as compared with Rayleigh-Benard convection. The convective flows in the experiment (Prandtl number = 5.17, $\mathrm{Ra} = 1.53\times10^5$, aspect ratio 2.0) were numerically simulated by three-dimensional computation. All the experimental and numerical results were arranged by Rayleigh number (Ra) and Nusselt number (Nu). In addition, we introduced the magnetic Rayleigh number ($\mathrm{Ra_m}$) instead of Ra. The results of Nu plotted versus the $\mathrm{Ra_m}$ were closely distributed in the vicinity of the Silveston curve. This relationship reveals that the heat transfer on magnetothermal convection is controlled by the use of $\mathrm{Ra_m}$.

DOI: 10.1103/PhysRevE.98.033109

I. INTRODUCTION

Magnetic force is a body force as well as a gravitational force [1,2]. The effect of gravity on thermal convection is canceled by a vertically upward magnetic body force, and thermal convection under a partial gravitational condition can be realized artificially on earth. In a similar way, thermal convection under a hypergravitational condition can be performed by the application of a downward magnetic body force. The driving body force of those convections originates from the resultant force between the gravitational force and the magnetic body force, and they are characterized as magnetothermal convection [3,4]. Recent studies of magnetothermal convection cover various scientific fields and applications [5–8]; in particular, heat transfer on the convection has progressed extensively by the introduction of the nondimensional parameter of the magnetic Rayleigh number ($\mathrm{Ra_m}$) [9–11]. The visualization of magnetothermal convection, however, is a challenging issue for many practical reasons, such as the narrowness of the space in the magnet bore and the difficulty of precise temperature control. So far, only a few experiments have succeeded in making observations. In one of these experiments, Nakamura *et al.* [12] visualized the transition process on convective flows enclosed in a shallow vessel which was made of transparent material, heated from below, and cooled from the top surface. They observed the process from the topside, and the change of convective cells in the Rayleigh-Benard model was continuously identified by adjusting the magnitude of magnetic body force from the condition of partial gravity to that of hypergravity. However, the observation from the upper side was inadequate for detecting the specific flows under a quasiweightless condition. Mogi *et al.* [13] visualized the thermal convection of water under strong gradient magnetic fields by pasting up a liquid-crystal sheet on the vessel sidewall, observing that the convection was significantly affected by the magnetic body force. But their results were indirectly deduced by the temperature distribution on the vessel sidewall, not by visualizing the flow regimes. Using an aqueous gadolinium nitrate solution and three-dimensional numerical computations, Maki *et al.* [14] previously investigated the thermal conductive state of the Rayleigh-Benard model in a quasiweightless condition, in which the heat transfer on convection was completely suppressed and the temperature difference between the heated and the cooled surfaces increased. Instead of experimental visualization, three-dimensional computations were conducted to estimate the thermal conductive state of convection [10,14].

In this study, we utilize a thermochromic liquid crystal (TLC) to visualize both the isothermal contours and the convective flows of magnetothermal convection in the magnet from the side view [15]. There have been some reports on the visualization of the Rayleigh-Benard convection by the

*makisyo@osaka-ohtani.ac.jp

TLC [16–22], but ours attempts to perform *in situ* observation of magnetothermal convection by the TLC. We develop an original observation system and equipment of the Rayleigh-Benard model, and measure the heat transfer on convection by varying the magnitude of the magnetic body force. A three-dimensional numerical simulation is also conducted to verify these phenomena.

II. EXPERIMENTS

A. Observation system

A schematic illustration of the apparatus is shown in Fig. 1. Figure 1(a) is the cylindrical superconducting magnet [JMTD-6T100EF3, Japan Superconductor Technology, Inc. (JASTEC)]. The origin of the coordinate system was defined at the center of the coil. The convection vessel [Fig. 1(b)] was horizontally positioned in two different locations at ±101 mm from the coil center. Figure 1 illustrates the vessel setup at $z_{\mathrm{coil}} = -101$ mm. The subscript *coil* means the aforementioned coordinate system of the coil. The vessel center coincided with the axis of the bore. The vessel sidewall was made of transparent acrylic (thickness 2 mm); the vessel's inner diameter (ID) was 20.0 mm, and the height was 12.0 mm. The vessel's top surface [Fig. 1(c)] was made of copper (3 mm thickness), and was uniformly cooled by water. This cooling-water circulated in the aluminum enclosure box [Fig. 1(d)], made contact with the top surface, and returned to a thermostat bath through nozzles [Fig. 1(e)]. A thermocouple [Fig. 1(f), T type, Anbe SMT Co., Ltd.] was inserted through a hole drilled in the top surface to reach the center of the vessel, where it could detect the temperature of the top surface of the vessel. The vessel's bottom surface [Fig. 1(g)] was also made of copper (3 mm thickness), and was uniformly heated by an electric heater [Fig. 1(h)] contained in an acrylic box [Fig. 1(i)] set under the bottom surface. The heating current was controlled by a DC power supply [Fig. 1(j), KX-100L, Takasago Co., Ltd.]. The bottom cover also had a drilled hole reaching to the center of the vessel, and the same type of thermocouple was attached to measure the temperature of the bottom. The temperature of the top and bottom surfaces was recorded with a data logger [Fig. 1(k), NR-1000, Keyence Co., Ltd.] at 1 min intervals. This entire system was mounted on a stable supporting stage [Fig. 1(l)]. Insulating material [Fig. 1(m)] was packed into the empty spaces in the system.

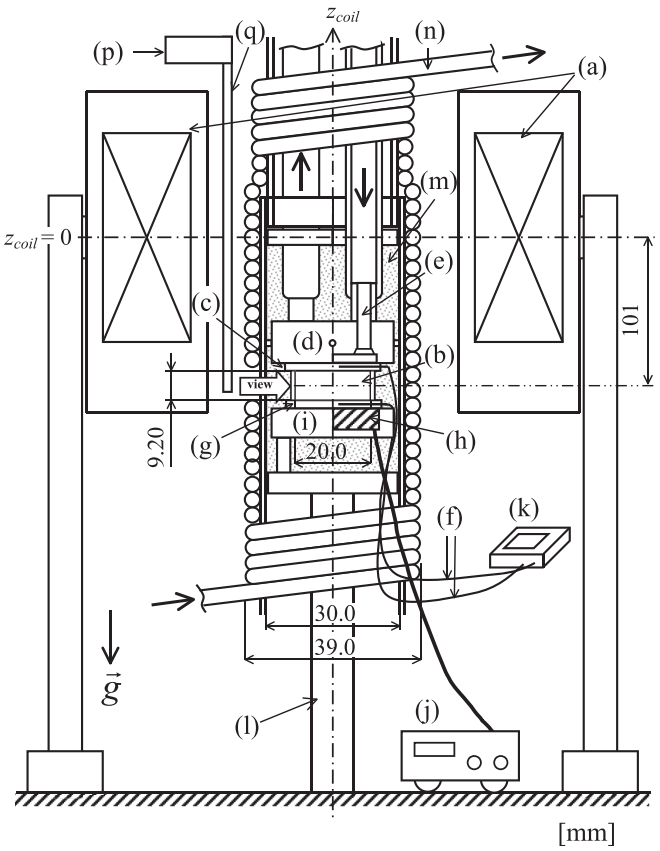

FIG. 1. Schematic illustration of the observation system and measurement equipment. (a) The cylindrical superconducting magnet. (b) The convection vessel horizontally located in the magnet. The vessel center coincides with the axis of the bore. The aspect ratio of the vessel (=ID/h_z) is 2.17. (c) The vessel's top surface made of copper (3 mm thickness). (d) The aluminum enclosure box. The cooling water circulates in this box and returns through a thermostat bath. (e) The nozzles on the enclosure box for the cooling water. (f) Thermocouples to detect the temperature of the top and bottom surfaces of the vessel. A hole drilled in the top cover reaches the vessel center and the thermocouple is inserted there. (g) The vessel's bottom cover made of copper (3 mm thickness). (h) The electric heater to uniformly heat the bottom surface. (i) The acrylic box to contain the heater. (j) DC power supply to control the heater. (k) The data logger to record the temperature. (l) The supporting stage. (m) Insulating material stuffed into the empty space of the system. (n) The water-looping system to control the temperature in the bore. (p) CCD camera. (q) A rigid scope.

Figure 2 shows photos of the observation system. Figure 2(a) shows the magnet and the visualization equipment. The lowercase letters in the figure correspond to those of the apparatus in Fig. 1. We can see the CCD camera [Fig. 1(p), OH414, Olympus Co., Ltd.] and part of the rigid scope [Fig. 1(q), Industrial Rigid Scope Type 5, Olympus Co., Ltd.].

Figure 2(b) is a closeup of the cylindrical vessel that induces the magnetothermal convection. The vessel [Fig. 1(a)] was fixed with three brass bolts extending between the top and the bottom surfaces. We inserted waterproofing rubbers (1 mm thickness) between the vessel sidewall and the top and bottom. A round convex step (19 mm diameter and 1 mm height) was attached to the surface so that the thickness of the rubbers

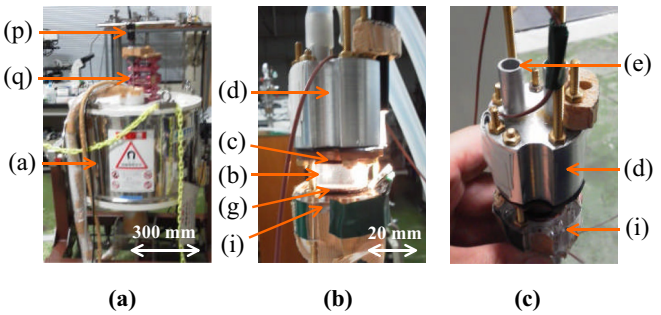

FIG. 2. Photos of the observation system. The lowercase letters in the figure correspond to those of the apparatus in Fig. 1. (a) The picture of the magnet and the visualization equipment. (b) The cylindrical vessel to induce the magnetothermal convection. (c) The aluminum enclosure box and the nozzles.

would not interfere with observation of the inside of the vessel. Owing to this step, the actual height of the vessel between the top and the bottom surfaces was 9.20 mm. This height was used as the standard length (h_z) in this study. The aspect ratio of the vessel ($= \mathrm{ID}/h_z$) was 2.17.

Figure 2(c) shows the aluminum enclosure box from Fig. 1(d) and the nozzles from Fig. 1(e). The temperature in the bore was controlled by a water-looping system [Fig. 1(n)]. In short, we used two thermostatic baths; one was used for cooling the top cover of the vessel, and the other was for maintaining the temperature in the bore.

B. Magnetic condition

We used an aqueous gadolinium nitrate solution of 0.15 mol/kg (pH = 4.52 at 305.5 °C) as the working fluid of convection. Gadolinium nitrate [$Gd(NO_3)_3 \cdot 6H_2O$, Wako Pure Chemical Industries, Ltd.] is a paramagnetic substance, and its aqueous solution is regarded as being homogeneous.

Figure 3 exhibits schematic illustrations of the conventional superconducting magnet and the magnetic conditions around the vessel. Figure 3(a) shows the location of the vessel.

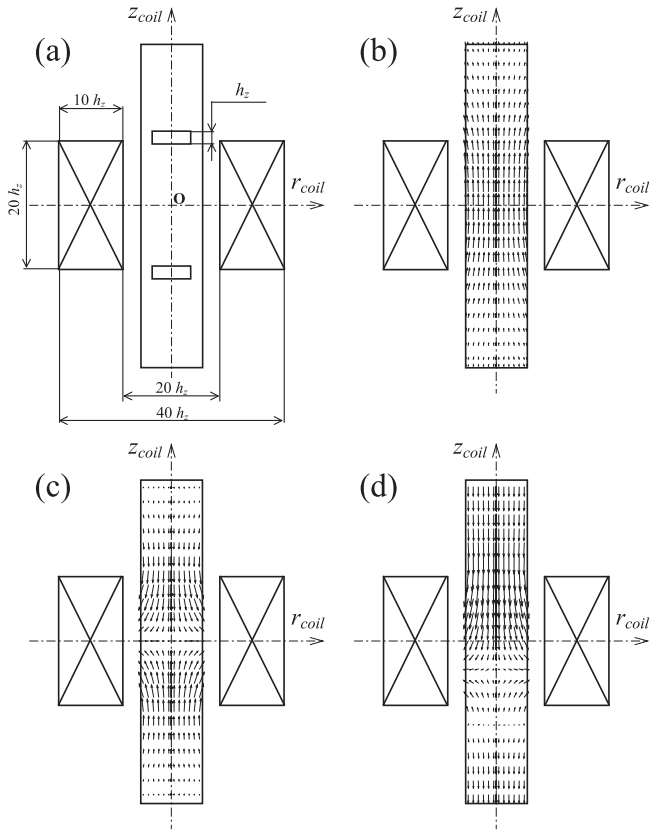

FIG. 3. Schematic illustrations of the conventional superconducting magnet and the magnetic conditions around the vessel. (a) The vessel location in a conventional superconducting magnet. (b) The distribution of the magnetic flux vectors $\vec{b} = (b_r, b_\phi, b_z)$. (c) The distribution of the magnetic body force vectors $\vec{f}_m = (f_{mR}, f_{mf}, f_{mZ})$, which act on a paramagnetic substance. (d) The quasiweightless condition is realized near the lower bore edge, and simultaneously the hypergravitational condition of two times the force of gravity is realized near the upper bore edge.

Figure 3(b) shows the distribution of the magnetic flux vectors $\vec{b} = (b_r, b_\phi, b_z)$ in the bore. Figure 3(c) is the distribution of the magnetic body force vectors $\vec{f}_m = (f_{mR}, f_{m\phi}, f_{mZ})$, which act on a paramagnetic substance. $\vec{b}$ and $\vec{f}_m$ are defined in a cylindrical coordinate system. Both vectors distribute axially symmetrically, and $\vec{f}_m$ is also symmetric with respect to the plane of $z_{\mathrm{coil}} = 0$. In the vicinity of the edge of the magnet coil, $\vec{f}_m$ directs vertically and the radial component of the magnetic body force (f_{mR}) becomes small. The vertical component of the magnetic body force (f_{mZ}) reaches its maximum value here. Figure 3(d) is the driving body force vectors combined between the magnetic body force and gravity when the magnitude of f_{mZ} is equal to that of gravity at the bore edge. In practice, the horizontal driving body force becomes the same as the horizontal magnetic body force since the radial and circumferential components of the gravity become zero. As a consequence, the driving body force vectors in Fig. 3(d) are presented vertically larger than those in Fig. 3(c). In this condition, a quasiweightless condition is realized near the lower bore edge, and a hypergravitational condition with two times the force of gravity is simultaneously realized near the upper bore edge, as shown in Fig. 3(d). The equations of the driving body force vectors will be specified in a later section.

In this study, we used a superconducing magnet that is capable of generating a maximum magnetic flux density of 6.0 T at the magnet center ($z_{\mathrm{coil}} = 0$, origin). The maximum $(\vec{b} \cdot \vec{\nabla})\, b_z$ on the bore axis was 333.24 T^2/m at $z_{\mathrm{coil}} = \pm 101$ mm. We set the vessel at $z_{\mathrm{coil}} = \pm 101$ mm in the experiments.

C. Visualization techniques

We utilized a thermochromic liquid crystal (Japan Capsule Products Co., Ltd.) at a concentration of 0.01 wt. % for the purpose of visualization. The thermochromic liquid crystal (TLC) became luminous in the temperature range of 30 to 40 °C; that is, a hot solution of 36–40 °C glows in purple or blue, a cold solution of 30–33 °C glows in red or yellow, and a medium temperature solution of 33–36 °C glows in green. The density of the TLC was close to that of water (∼1.01−1.02), and its particulate size was about 10–20 μm. We adjusted the power of the heater so that the solution temperature became stable between 30 and 40 °C.

Lighting was indispensable in the dark magnet bore. The direction of the lighting was optimized so that the luminescence of the TLC could be perfectly perceived. The solution was lightened diagonally about 45° from the viewpoint of the camera.

III. RESULTS

A. *In situ* observation

Figure 4 shows photos of the convective flows from the side view. Figure 4(a) shows the conventional convection without applying the magnetic field. The isothermal illuminant of the TLC was not visualized in the case of the Rayleigh-Benard convection. Figures 4(b) and 4(c) show the magnetothermal convection when the magnetic flux density of 3.00 T was applied at $z_{\mathrm{coil}} = 0$. Figure 4(b) is the case when the vessel was located at the position of $z_{\mathrm{coil}} = +101$ mm, and Fig. 4(c) is the case at $z_{\mathrm{coil}} = -101$ mm. The magnitudes of b_z and $|(\vec{b} \cdot \vec{\nabla})b_z|$

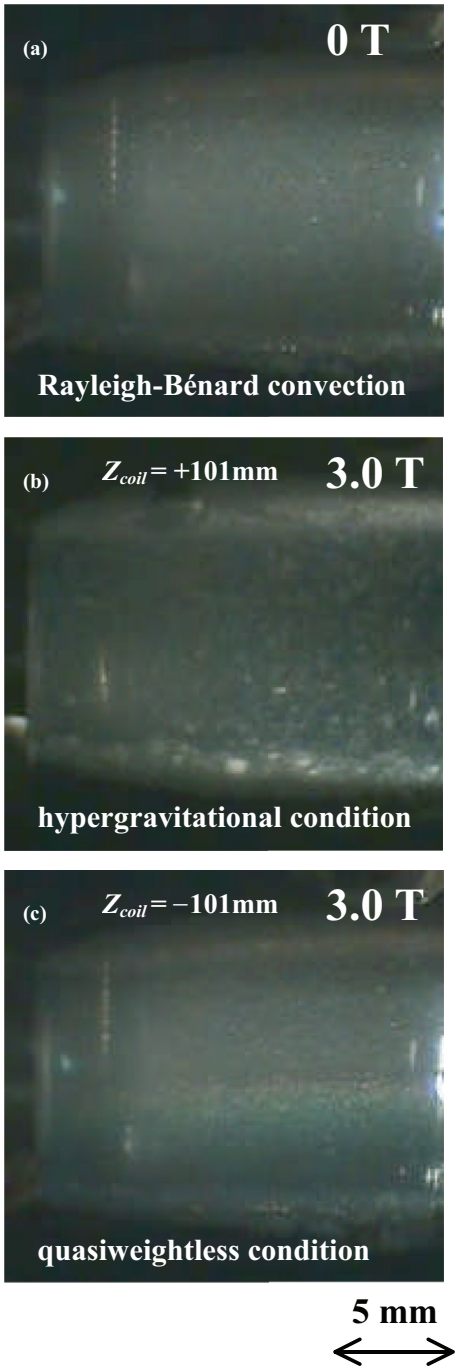

FIG. 4. Photos of the convective flows from the side view. (a) The Rayleigh-Benard convection without applying the magnetic field. (b) and (c) show the magnetothermal convection. The applied magnetic flux density is 3.0 T. The magnitudes of b_z and $|(\vec{b}\cdot\vec{\nabla})b_z|$ at $z_{\rm coil} = \pm 101$ mm correspond to 2.12 T and 83.31 T^2/m, respectively. We can notice small particulates moving in the photos. These particulates are the aggregated TLC. The photo in (c) shows that the horizontal isothermal illuminant of the TLC appears at $z_{\rm coil} = -101$ mm. This illuminant identifies that the upward magnetic body force cancels the effect of gravity and the thermal conductive state is certainly realized. On the other hand, when the vessel is located at the position of $z_{\rm coil} = +101$ mm, no illuminant appears at all, as shown in (b).

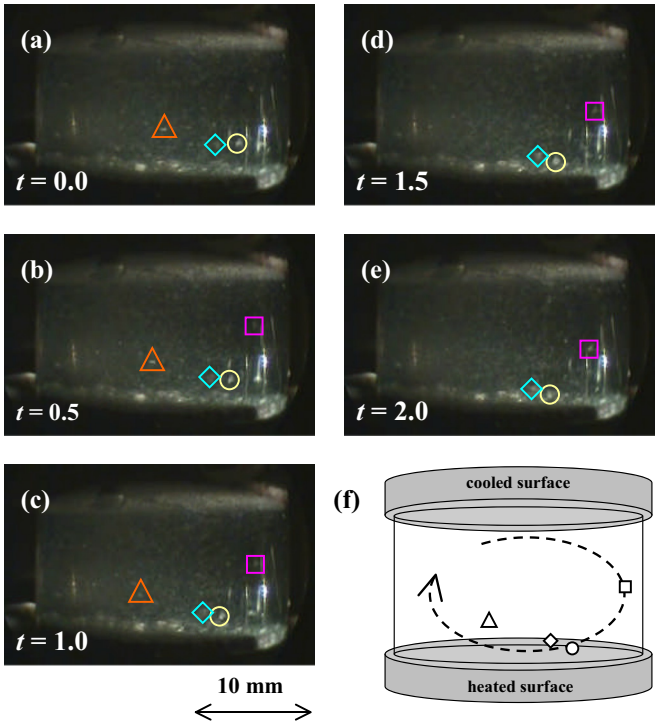

FIG. 5. The sequence of photographs of the particulates of the aggregated TLC under the hypergravitational condition by 0.5 s. Some of the particulates are characterized by the circles, diamonds, triangles, and squares in the photographs. We can find that one large roll occurs in the vessel by tracing the particulates in (a)–(e). As far as we can see, the speed is 0.2–1.0 mm/s. This roll and the particulates are schematically illustrated in (f).

at $z_{\rm coil} = \pm 101$ mm corresponded to 2.12 T and 83.31 T^2/m, respectively. When the vessel was at $z_{\rm coil} = +101$ mm, however, the illuminant did not appear at all, as shown in Fig. 4(b). The horizontal isothermal illuminant of TLC appeared for the first time in Fig. 4(c), proving by this illuminant that the upward magnetic body force canceled the effect of gravity and that a thermal conductive state was certainly realized.

We noticed small moving particulates of aggregated TLC in the solution. The sequence of photographs every 0.5 s in Fig. 5 traces some of the particulates under the hypergravitational condition. They are characterized by the circles, diamonds, triangles, and squares in the photographs, and the speed of the flows was estimated to be 0.2–1.0 mm/s. In Fig. 5, we found one large roll that occurred in the vessel. That roll and the particulates are schematically illustrated in Fig. 5(f). A similar convective roll was observed in the case of Rayleigh-Benard convection in Fig. 4(a), the speed of which was close to that of the hypergravitational condition. In contrast, the flow regimes of the thermal conductive state in Fig. 4(c) were conclusively different from those of the convections, with a speed of less than 0.02 mm/s.

The horizontal illuminant appeared five and more minutes after the particulates' movement had stopped. The slowness of the illuminant was one of the major difficulties in visualizing

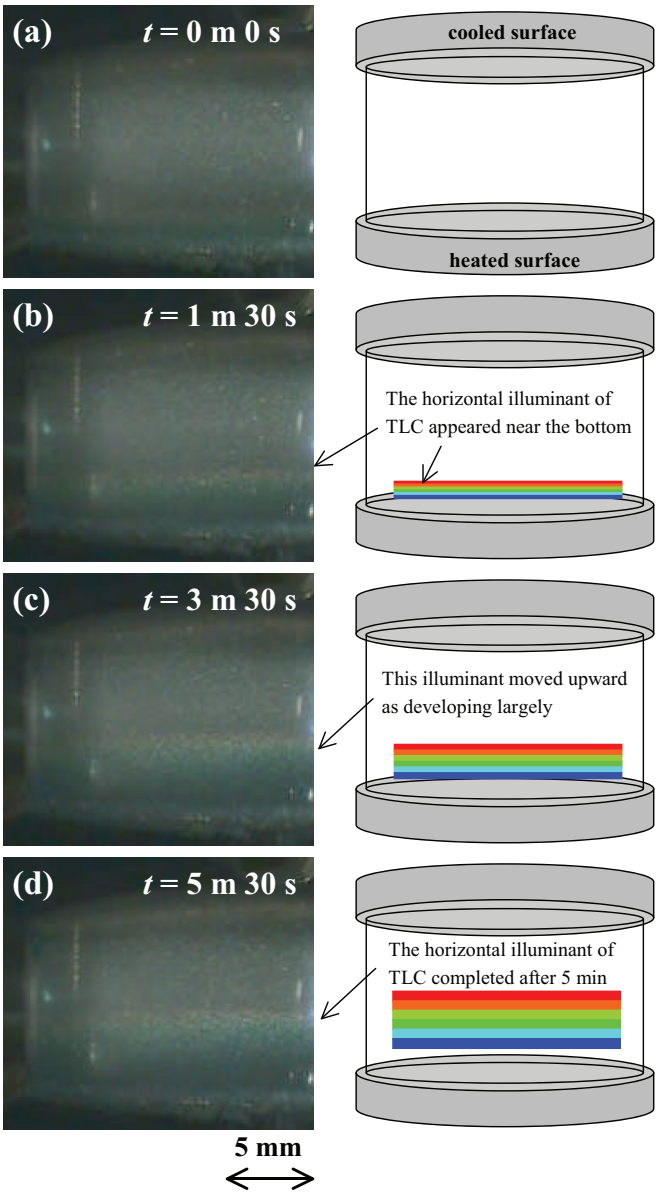

FIG. 6. A sequence of photographs of the developing process of the horizontal illuminant of the TLC, with schematic illustrations. The illuminant appears five or more minutes after the particulates' movement has stopped. The illuminant first appears in the vicinity of the bottom surface and moves upward to the vessel center as it increases in size.

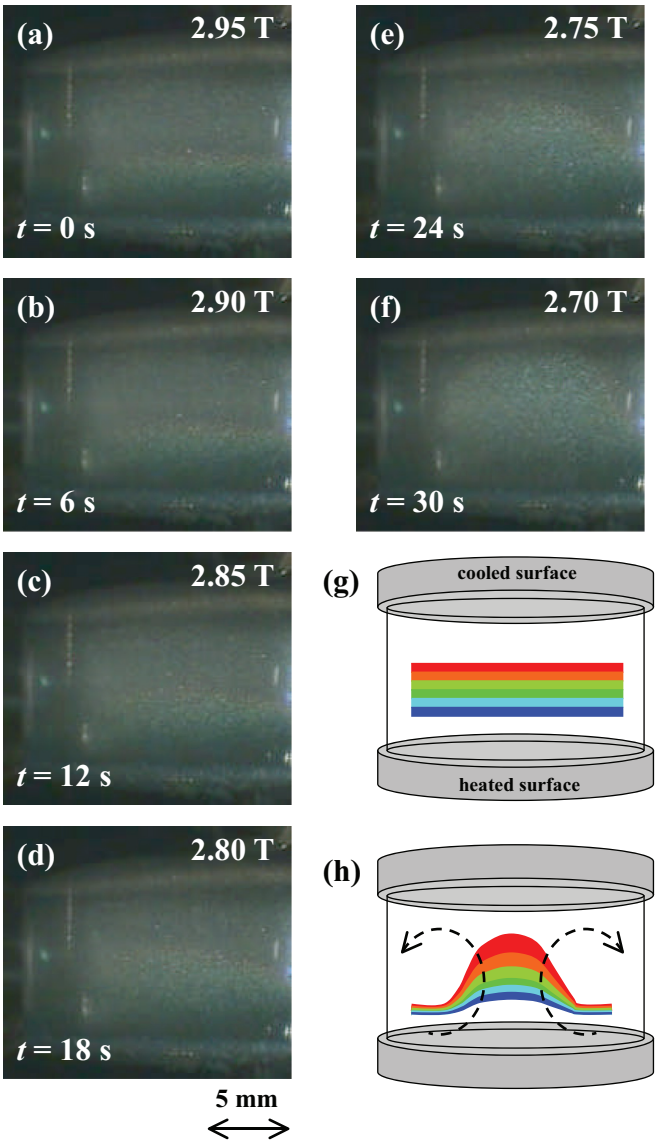

FIG. 7. The breaking process of the horizontal illuminant when the magnetic flux density is 3.0 T is gradually weakened from 2.95 T to 2.70 T at $z_{\mathrm{coil}} = 0$. The thermal conductive state is maintained when it is between (a) 2.95 and (b) 2.90 T. (c) The critical moment when the conductive state breaks at 2.85 T. $|(\vec{b}\cdot\vec{\nabla})b_z|$ is 75.19 T^2/m at $z_{\mathrm{coil}} = -101$ mm. (d)–(f) show the process in which the initial horizontal illuminant is curved by the rising upward flows. After the breaking, one large roll occurs by the observation of the particulates. (g) and (h) schematically illustrate the steady horizontal illuminant and its breaking process, respectively.

the magnetothermal convection. The sequence of photographs in Fig. 6, accompanied by schematic illustrations, represents the developing process of the illuminant. The illuminant first appeared in the vicinity of the bottom surface [Fig. 6(b)] and moved slowly to the vessel center as it increased in size [Figs. 6(c) and 6(d)]. This process will be discussed in a later section with the results of three-dimensional numerical computations.

The sequence of photographs in Fig. 7 shows the breaking process of the horizontal illuminant when the magnetic flux density was gradually weakened from 2.95 T to 2.70 T at $z_{\mathrm{coil}} = 0$. The initial state was maintained from 2.95 to 2.90 T [see Figs. 7(a) and 7(b)]. Figure 7(c) shows the moment when the conductive state is broken at 2.85 T. When at 2.85 T, $|(\vec{b}\cdot\vec{\nabla})b_z|$ was 75.19 T^2/m at $z_{\mathrm{coil}} = -101$ mm. Figures 7(d)–7(f) clarify the process in which the initial horizontal illuminant was curved by the upward flows and instantly formed a convex distribution. Figures 7(g) and 7(h) schematically illustrate the stable horizontal illuminant and its breaking process, respectively.

After the break of the conduction state, the horizontal illuminant disappeared quickly. This means that the illuminant of the TLC was sensitive to the flows. By using the

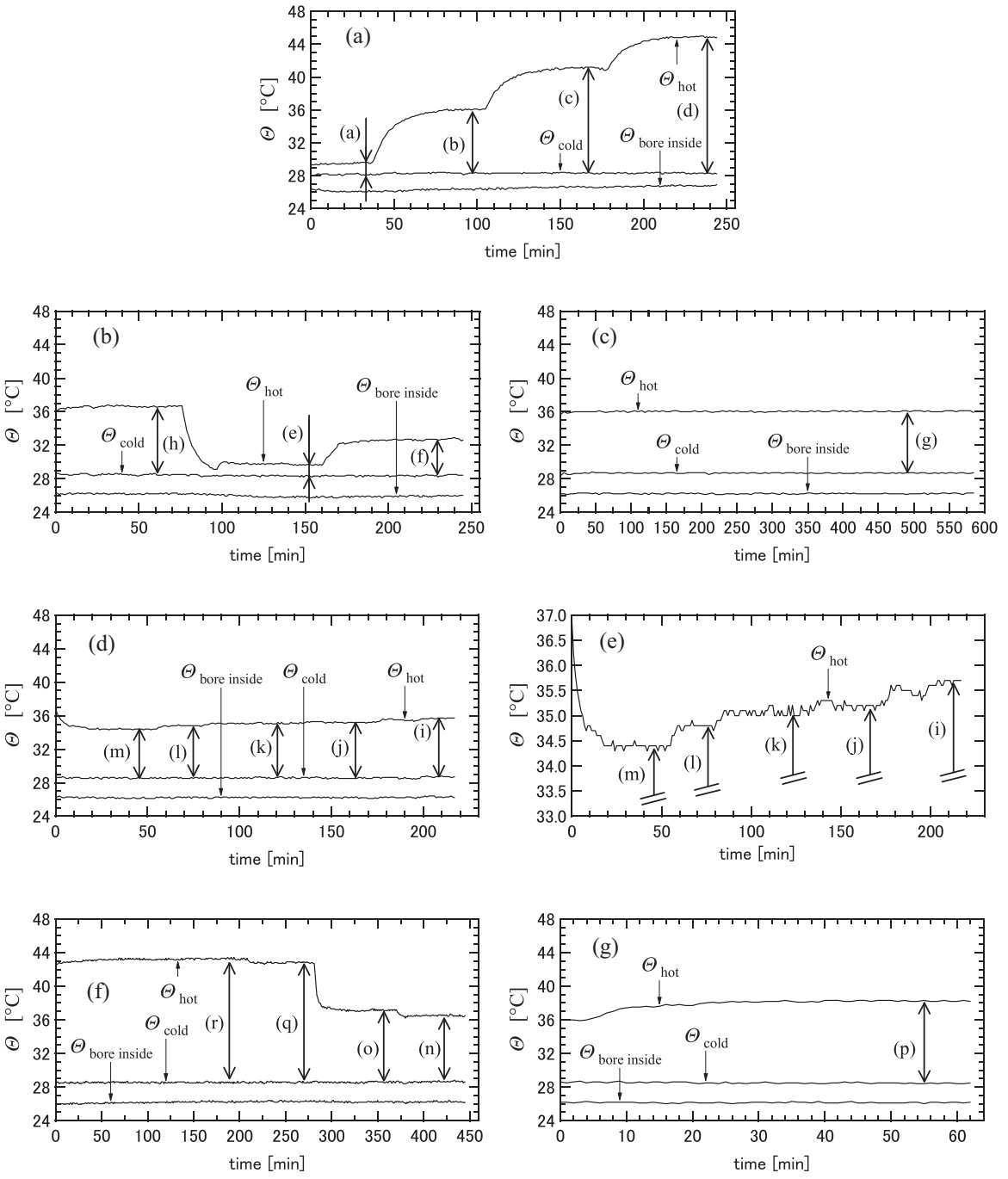

FIG. 8. Chronological responses of Θ_{hot} and Θ_{cold} measured at 1 min intervals. (a) is the responses under the thermal conductive state. (b) and (c) are those without applying the magnetic field in the Rayleigh-Benard model. (d) and (e) are the responses under the hypergravitational condition. (e) is the partial enlargement of (d). (f) and (g) are the responses under the partial gravitational condition. The symbols from (a) to (r) schematically represent the $\Delta\Theta$ when Θ_{hot} and Θ_{cold} became thermally steady. We use the steady data of $\Delta\Theta$ in the analysis. Table I exhibits the averaged results of Θ_{hot}, Θ_{cold}, $\Delta\Theta$, and Q_{supply}. The number of data utilized in the analysis is also listed in this table.

particulates as the tracer, we found that the flows changed into a large, nonaxisymmetric roll, which is similar to the Rayleigh-Benard convection in Fig. 4(a). The breaking process will be discussed later to estimate the critical condition. Short movies of Figs. 4(a), 6, and 7 are available in the Supplemental Material [23].

B. Heat transfer of the system

The heat transfer of the system was examined by a method developed by Churchill and Ozoe [24]. This method is a practical technique to accurately estimate the amount of heat loss in an overall system. In the first step, the initial arrangement of the vessel (Rayleigh-Benard model) was turned upside down

in the bore, and the top surface of the vessel was heated while the bottom one was cooled. In such an arrangement, a low-density solution that has been heated stays in the upper part of the vessel, and a high-density solution that has been cooled stagnates in the lower part. Consequently, a physically stable condition in density is formed and hardly any convective flows are induced. This condition is exactly the same as the thermal conductive state. Under this condition, the heat transfer of thermal conduction $Q_{\rm cond}$ (W) can be analytically calculated by using Fourier's heat-conductive equation [25] as

$$Q_{\rm cond} = A\lambda\frac{\partial\Theta}{\partial x} \cong A\lambda\frac{\Theta_{\rm hot}-\Theta_{\rm cold}}{h_z}. \quad (1)$$

Here, A, λ, Θ, and h_z are the square measure of the vessel (m^2), thermal conductivity W/(m K), temperature (K), and the practical interval between the vessel surfaces (m). The subscripts *hot* and *cold* mean the hot and the cold surfaces of the vessel, respectively.

We measured the temperature difference $\Delta\Theta$ ($=\Theta_{\rm hot}-\Theta_{\rm cold}$) by changing the amount of supplied power $Q_{\rm supply}$ (W). Figure 8 shows the chronological responses of $\Theta_{\rm hot}$ and $\Theta_{\rm cold}$ measured at 1 min intervals. The symbols (a) to (r) in the figures schematically represent the $\Delta\Theta$ when the responses became thermally steady. We used the steady data of $\Delta\Theta$ in the analysis. Table I exhibits the averaged results of $\Theta_{\rm hot}$, $\Theta_{\rm cold}$, $\Delta\Theta$, and $Q_{\rm supply}$. The number of data utilized in the analysis is also listed in this table. Figure 8(a) shows the responses under the thermal conductive state. The correlation between $\Delta\Theta$ and $Q_{\rm supply}$ is plotted with the diamond symbol in Fig. 9. This correlation became a linear function, and is expressed with the straight line (A) written as $\Delta\Theta = 17.395\,Q_{\rm supply}$. The R^2 value of the line (A) was 0.9987.

The heat loss $Q_{\rm loss}$ (W) was obtained by subtracting the amount of $Q_{\rm cond}$ (W) from the amount of $Q_{\rm supply}$:

$$Q_{\rm loss} = Q_{\rm supply} - Q_{\rm cond}. \quad (2)$$

The correlation of $\Delta\Theta$ and $Q_{\rm loss}$ also becomes a linear function. The straight line is shown with the dot-dashed line (B) in Fig. 9. The line (B) was obtained by horizontally making a subtraction of $Q_{\rm cond}$ from the line (A), and was derived by $\Delta\Theta = 27.666\,Q_{\rm supply}$. The R^2 value of the line (B) was 0.9999.

Next, the vessel was returned to the situation for the Rayleigh-Benard model, with the heated surface on the bottom and the cooled surface on the top. Then we measured the correlation between the averaged $\Delta\Theta$ and $Q_{\rm supply}$ in a similar fashion. Figures 8(b) and 8(c) are the chronological responses of $\Theta_{\rm hot}$ and $\Theta_{\rm cold}$ measured at 1 min intervals. These data are plotted by the circle symbol in Fig. 9, where the correlation is presented by the dashed line (C). This line was derived by $\Delta\Theta = 8.2129\,Q_{\rm supply} + 0.3572$ ($Q_{\rm supply} \geqslant 0.1434$), and the R^2 value of the line (C) was 0.9983.

In the vessel, the heat transfer $Q_{\rm heat-transf}$ (W) was calculated by the following equation:

$$Q_{\rm heat-transf} = Q_{\rm supply} - Q_{\rm loss}. \quad (3)$$

TABLE I. Experimental results of the measurements.

	$Q_{\rm supply}$ (W)	b_z[a] (T)	$Q_{\rm hot}$ + SD[b] (°C)	$Q_{\rm cold}$ + SD (°C)	$\Delta\Theta$ (K)	Ave. Θ[c] (°C)	N[d]	Symbols in Fig. 8
Cond.[e]	0.0816	0	29.51 ± 0.08	28.15 ± 0.07	1.36	28.83	21	(a)
	0.4620	0	36.03 ± 0.08	28.28 ± 0.06	7.75	32.16	24	(b)
	0.7142	0	41.14 ± 0.06	28.29 ± 0.06	12.85	34.72	18	(c)
	0.9632	0	44.87 ± 0.07	28.29 ± 0.07	16.58	36.58	29	(d)
RB[f]	0.1434	0	29.78 ± 0.05	28.34 ± 0.06	1.44	29.06	28	(e)
	0.4620	0	32.68 ± 0.11	28.38 ± 0.08	4.30	30.53	34	(f)
	0.8475	0	36.03 ± 0.06	28.65 ± 0.05	7.38	32.34	107	(g)
	0.9632	0	36.64 ± 0.08	28.48 ± 0.07	8.16	32.56	46	(h)
MC + 101 mm[g]	0.8475	1.5	35.59 ± 0.13	28.63 ± 0.11	6.96	32.11	27	(i)
		2.1	35.19 ± 0.05	28.52 ± 0.05	6.66	31.86	29	(j)
		2.5	35.07 ± 0.07	28.57 ± 0.07	6.50	31.82	37	(k)
		2.9	34.80 ± 0.03	28.55 ± 0.05	6.25	31.68	18	(l)
		4.0	34.39 ± 0.04	28.54 ± 0.06	5.85	31.46	27	(m)
MC −101 mm	0.8475	1.5	36.49 ± 0.08	28.64 ± 0.07	7.86	32.57	56	(n)
		2.1	37.13 ± 0.08	28.57 ± 0.08	8.56	32.85	56	(o)
		2.5	38.22 ± 0.07	28.47 ± 0.06	9.75	33.35	37	(p)
		2.9	43.24 ± 0.09	28.54 ± 0.07	14.70	35.89	28	(q)
		4.0	43.21 ± 0.07	28.54 ± 0.06	14.67	35.88	75	(r)

[a] b_z: Vertical component of magnetic flux density (T = Wb/m^2 = $V\,s/m^2$).
[b] SD: Standard deviation.
[c] Ave. Θ: Averaged temperature Θ (°C).
[d] N: The number of data measured by 1 min.
[e] Cond.: Conductive state.
[f] RB: Rayleigh-Benard convection.
[g] MC: Magnetothermal convection.

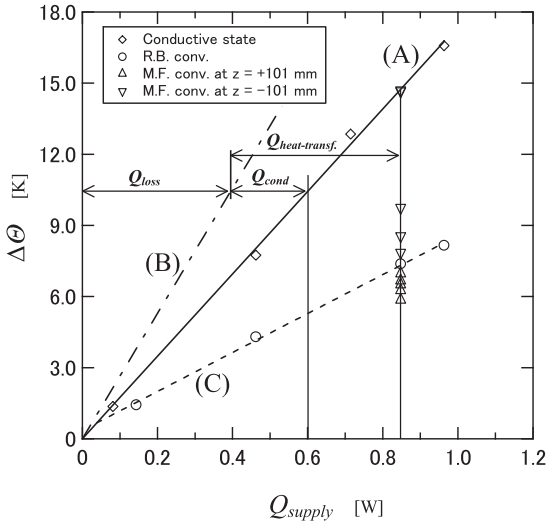

FIG. 9. Correlation of the temperature difference $\Delta\Theta$ and the thermal energy of Q_{supply}, Q_{cond}, and Q_{conv}. The solid line (A) shows the linear function of $\Delta\Theta$ and Q_{supply} in the thermal conductive model. The dot-dashed line (B) is the correlation of $\Delta\Theta$ and Q_{loss}. The horizontal distance between lines (B) and (A) is equal to the magnitude of Q_{cond}, and the amount of Q_{cond} is obtained by the Fourier heat-conductive equation. Consequently, line (B) is estimated analytically. The dashed line (C) shows the correlation of $\Delta\Theta$ and Q_{supply} in the Rayleigh-Benard model. Q_{loss}, Q_{cond}, and $Q_{\text{heat-transf}}$ are schematically represented in this figure. The heat transfer $Q_{\text{heat-transf}}$ is calculated by $Q_{\text{heat-transf}} = Q_{\text{cond}} + Q_{\text{conv}}$, and Nu is defined by the ratio of $Q_{\text{heat-transf}}$ to Q_{cond} in this figure. The diamond symbol is the experimental data measured under the thermal conductive state. The circle symbol is the experimental data measured under the Rayleigh-Benard model without applying the magnetic body force. The triangle symbol is the experimental data measured under the hypergravitational condition at $z_{\text{coil}} = +101$ mm. The reversed triangle symbol is the experimental data measured under the partial gravitational condition at $z_{\text{coil}} = -101$ mm. In this study, Q_{supply} was kept at 0.8475 W so that the solution temperature became stable between 30 and 40 °C. The magnetic flux density was varied as 4.000, 2.900, 2.500, 2.100, and 1.500 T at $z_{\text{coil}} = 0$. The absolute values of those magnitudes of $|(\vec{b}\cdot\vec{\nabla})b_z|$ at$z_{\text{coil}} = \pm 101$ mm correspond to 148.11, 77.85, 57.85, 40.82, and 20.83 T^2/m. All the experimental results of Nu are summarized in Table II.

On the other hand, $Q_{\text{heat-transf}}$ can also be defined by the heat transfer of thermal convection Q_{conv} (W):

$$Q_{\text{heat-transf}} = Q_{\text{cond}} + Q_{\text{conv}}. \tag{4}$$

The Nusselt number (Nu) is defined by the ratio of $Q_{\text{heat-transf}}$ to Q_{cond}, in the following equation:

$$Nu = \frac{Q_{\text{heat-transf}}}{Q_{\text{cond}}} \geqslant 1.0. \tag{5}$$

The values of Q_{loss}, Q_{cond}, and $Q_{\text{heat-transf}}$ are schematically illustrated by the length of the projection lines in Fig. 9. The horizontal distance between the lines of (A) and (B) represents the magnitude of Q_{cond}. Nu is experimentally estimated by the ratio of the amounts of $Q_{\text{heat-transf}}$ and Q_{cond} in Fig. 9. In the Rayleigh-Benard model, $\Delta\Theta$ becomes smaller than that in the state of thermal conduction because the heat transfer of $Q_{\text{heat-transf}}$ is larger than that of Q_{cond}. Therefore, Nu is always larger than 1.0.

TABLE II. Experimental results of heat transfer. Q_{supply} was 0.8475 W constant.

	B (T)	Pr	Ra	Ra_{m}[a]	Nu	Symbols in Fig. 8
RB	0.0	5.51	25710	25710	2.97	(e)
		5.36	82059	82059	3.34	(f)
		5.17	152550	152550	3.69	(g)
		5.15	170337	170337	3.84	(h)
MC +101 mm	1.5	5.20	142412	188807	4.01	(i)
	2.1	5.22	134838	220938	4.27	(j)
	2.5	5.22	131294	250109	4.42	(k)
	2.9	5.24	125498	278319	4.66	(l)
	4.0	5.26	116408	386090	5.09	(m)
MC −101 mm	1.5	5.15	164027	110589	3.36	(n)
	2.1	5.12	180839	65366	2.95	(o)
	2.5	5.07	210508	20007	2.38	(p)
	2.9	4.81	354012	−77073	1.01	(q)
	4.0	4.81	352910	−464675	1.01	(r)

[a]Ra_{m} was calculated with the critical magnetic flux density of 2.63 T.

All the experimental results of Nu are summarized in Table II. In this study, Q_{supply} was kept at 0.8475 W so that the solution temperature became stable between 30 and 40 °C. The magnetic flux density was varied as 4.000, 2.900, 2.500, 2.100, and 1.500 T at $z_{\text{coil}} = 0$, which correspond to 2.826, 2.049, 1.767, 1.484, and 1.060 T at $z_{\text{coil}} = \pm 101$ mm, respectively. The absolute values of these magnitudes of $|(\vec{b}\cdot\vec{\nabla})b_z|$ at $z_{\text{coil}} = \pm 101$ mm were 148.11, 77.85, 57.85, 40.82, and 20.83 T^2/m, respectively. Figures 8(d) and 8(e) are the chronological responses of Θ_{hot} and Θ_{cold} under the hypergravitational condition at $z_{\text{coil}} = +101$ mm. Figure 8(e) is a partial enlargement of Fig. 8(d). Figures 8(f) and 8(g) are the response under the partial gravitational condition at $z_{\text{coil}} = -101$ mm.

In Fig. 9, the data under the partial gravitational condition are plotted by the reversed triangles, and the data under the hypergravitational condition are plotted by the triangles. Under the partial gravitational condition, $\Delta\Theta$ became larger than that in the case of Rayleigh-Benard convection since the heat transfer was suppressed. Under the hypergravitational condition, $\Delta\Theta$ became smaller than that in the case of Rayleigh-Benard convection since the heat transfer was promoted. When the magnetic flux density was 2.90 T, the reversed triangle symbol was reached on the line (A). This means that the quasiweightless condition was realized magnetically.

IV. NUMERICAL COMPUTATIONS

A. Equations

The three-dimensional numerical computations of magnetothermal convection of paramagnetic liquids were shown in previous reports [14–16]. The magnetic body force is proportional to the volumetric magnetic susceptibility χ_v (dimensionless). Here, χ_v is defined as $\chi_v = \rho\chi_m$, where ρ is the subject density (kg/m^3), and χ_m is the mass magnetic susceptibility

(m^3/kg). In the case of a diamagnetic liquid, the magnitude of the magnetic body force is proportional to ρ since χ_m becomes almost constant. Hence, only density inhomogeneity by the temperature causes the driving body force of magnetothermal convection. In the case of a paramagnetic liquid, the effect of Curie's law [26] is superimposed on the driving body force. That is, χ_m is inversely proportional to the absolute temperature by Curie's law, and ρ also changes by the temperature.

In the numerical computations in this study, we adopted the Boussinesq approximation to ρ. With a reference density ρ_0 and a reference volumetric coefficient of expansion β_0 at the representative temperature Θ_0, the density ρ is calculated as

$$\rho = \frac{\rho_0}{1 + \beta_0 (\Theta - \Theta_0)}. \tag{6}$$

Maki *et al.* established the momentum equation of paramagnetic fluids by which the magnetic body force term and the gravitational force term were integrated into one term [14]. This equation was successfully nondimensionalized by using the techniques of Hellums and Churchill [27]. As mentioned before, the vessel interval (= actual vessel height 9.2 mm) was used as the standard length (h_z) on the nondimensionalization. In the process of nondimensionalization, a dimensionless parameter C was utilized for a paramagnetic liquid. This parameter contains both the effects of Curie's law and the change of density by temperature, and is defined as follows:

$$C = 1 + \frac{1}{\beta_0 \Theta_0}. \tag{7}$$

Here, β_0 is the volumetric coefficient of expansion at the temperature Θ_0, i.e., 32.34 °C (Θ_0 = 305.5 K). The value of C became 11.5 in this study (see Appendix A). In practice, C is a coefficient that enhances the magnitude of the magnetic body force magnitude when the nondimensionalized momentum equations are computed.

In a manner similar to Hellums and Churchill's method, the equation of continuity and the equation of energy balance were also nondimensionalized. Equations (8)–(10) are the nondimensionalized equations of continuity, the nondimensionalized momentum equation for the paramagnetic liquid, and the nondimensionalized equation of energy balance, respectively. Equation (11) is the nondimensionalized Biot-Savart law. Equations (8)–(11) were computed on the cylindrical coordinate system:

$$\vec{\nabla} \cdot \vec{U} = 0, \tag{8}$$

$$\frac{D\vec{U}}{D\tau} = -\vec{\nabla} P + \mathrm{Pr}\nabla^2 \vec{U} + \mathrm{Ra} \times \mathrm{Pr} \times T \times \left[\begin{pmatrix} 0 \\ 0 \\ 1 \end{pmatrix} - \gamma \frac{C}{2} \vec{\nabla} (\vec{B})^2 \right], \tag{9}$$

$$\frac{DT}{D\tau} = \nabla^2 T, \tag{10}$$

$$\vec{B} = -\frac{1}{4\pi} \oint \frac{\vec{R} \times d\vec{S}}{|\vec{R}|^3}. \tag{11}$$

In these equations, $\vec{\nabla}$ and $\vec{U}$ are nabla (differential operator) and nondimensionalized velocity vector (U, V, W), respectively. T, P, τ, ∇^2, Pr, and Ra are nondimensionalized temperature, pressure, time, Laplacian (differential operator), Prandtl number ($\mathrm{Pr} = \frac{\nu}{\alpha}$), and Rayleigh number ($\mathrm{Ra} = \frac{g\beta(\Theta_{\mathrm{hot}} - \Theta_{\mathrm{cold}})h_z^3}{\alpha\nu}$), respectively. Here, α, ν, and g are thermal diffusivity (m^2/s), kinematic viscosity (m^2/s), and gravitational acceleration (m/s^2), respectively. The dimensionless parameter γ represents the magnitude of the magnetic body force [9–11,14,28], defined as $\gamma = \frac{\chi_v {b_a}^2}{\mu_0 \rho_0 g h_z}$. Here, ρ_0 is the reference density of the solution at Θ_0 (= 305.5 K), and was approximated with the density of water at this temperature (994.9 kg/m^3) [29]. b_a is the representative magnetic flux density defined as $b_a = \mu_0 i / h_z$ (T), where i and μ_0 are the electric current in a coil (A) and the magnetic permeability in vacuum $4\pi \times 10^{-7}$ (H/m), respectively. In Eq. (11), $d\vec{S}$ is the dimensionless position vector on the coil and $\vec{R}$ is $\vec{R} = (R, \theta, Z)$. $\vec{B} = (B_r, B_\theta, B_z)$ is the nondimensionalized magnetic flux vector. The magnitude of γ was defined at the representative point of the vessel center.

Equations (8)–(11) were discretized with the equal-interval staggered grid. We utilized the highly simplified marker and cell (HSMAC) method and solved the equations by the explicit method [30]. On the right-hand side of Eq. (9), the fist term represents the pressure, the second term the viscosity resistance, and the third term the effect of gravity. Notice that the magnitude of the nondimensionalized gravity becomes 1.0. The fourth term represents the magnetic body force, and is combined with the third term by using Pr and Ra. Actually, the square brackets in the last term (the third and fourth terms) give the driving body force vector on convection.

In the numerical computations, Pr and Ra were fixed as 5.17 and 1.53×10^5, respectively (see Appendix A). The aspect ratio of the vessel was decided as 2.0. The influence of the Lorentz force was ignored since the Hartmann number (Ha) was in the range of 0.62 to 0.68 (see Appendix A). These parameters were established on the basis of the experimental results of Rayleigh-Benard convection when the Q_{supply} was 0.8475 W. In this study, actual convective flows were numerically verified as varying with the magnitude of the magnetic body force.

B. Boundary conditions for the computations

We assumed that the boundary conditions of velocity were completely solid. The boundary conditions of temperature were as follows: the top surface is cold [Eq. (12)], the bottom hot [Eq. (13)], and the sidewall adiabatic [Eq. (14)]. The initial conditions in Eq. (15) were only used in the case of computation of the Rayleigh-Benard convection. In the cases of magnetothermal convection, the result of the Rayleigh-Benard convection was used as the initial condition:

$$\text{at the vessel top surface } (Z = +0.5), \quad \vec{U} = \vec{0}, \quad T = -0.5, \tag{12}$$

$$\text{at the vessel bottom surface } (Z = -0.5), \quad \vec{U} = \vec{0}, \quad T = +0.5, \tag{13}$$

TABLE III. Computations to verify the grid size (Pr = 5.17, Ra = 1.53×10^5).

NR	NTH	NZ	Ave. $U \pm$ SD	Ave. $V \pm$ SD	Ave. $W \pm$ SD	Nu $\pm$ SD
21	33	31	40.65 ± 3.82	47.66 ± 4.09	47.66 ± 3.25	5.05 ± 0.23
26	41	31	41.66 ± 3.82	47.47 ± 4.18	46.99 ± 2.90	5.00 ± 0.22
31	61	41	41.70 ± 3.27	47.61 ± 3.93	46.81 ± 2.54	4.77 ± 0.21
31	61	43	41.56 ± 3.59	47.42 ± 4.56	46.96 ± 3.12	4.76 ± 0.20
31	61	46	41.49 ± 3.18	47.30 ± 4.15	46.76 ± 2.74	4.71 ± 0.20
31	61	51	41.70 ± 3.33	47.38 ± 4.51	46.63 ± 2.61	4.68 ± 0.18

$$\text{at the vessel sidewall } (R = 1.0), \quad \vec{U} = \vec{0}, \quad \frac{\partial T}{\partial R} = 0, \tag{14}$$

$$\text{at} \quad \tau = 0, \quad \vec{U} = \vec{0}, \quad T = 0. \tag{15}$$

Nu was computed at the $Z = +0.5$ plane (i.e., cold surface).

C. Grid size for the computations

To adopt the proper grid size for the computations, preliminary numerical computations of Rayleigh-Benard convection (Pr = 5.17 and Ra = 1.53×10^5) were carried out with different grid sizes. Table III shows the velocity components of the averaged U, V, and W calculated on the whole grid and the averaged Nu. None of the preliminary computations changed to steady flows since Ra was too large to make the flows stable. According to the results, the grid numbers for the radial (NR), circumferential (NTH), and axial (NZ) directions were decided as 31, 61, and 46, respectively. Figures 10(a) and 10(b) show the cross-sectional views of the grid at the $Z = 0$ and $Y = 0$ planes, respectively. Figure 10(c) is a crane shot of the grids.

D. Rayleigh-Benard convection

Figure 11 shows the Rayleigh-Benard convection calculated with the grid size mentioned above. This result was used as the initial condition for all the computations of magnetothermal convections. Figure 11(a) shows the horizontal cross-sectional isothermal distribution at the $Z = 0$ plane. The hot solution rises where the distribution is in red or yellow, and the cold solution falls where it is in blue. Figures 11(b) and 11(c) show the vertical cross-sectional isothermal and velocity distributions at the $Y = 0$ plane and $X = 0$ plane, respectively. As a result, we notice that large rolls occur, similar to the flow regimes seen in the experiment [Fig. 4(a)].

E. Magnetic body force in the vessel

The magnetic body force in the vessel was calculated after the grid size was determined. In the computation, the magnet coil was approximated to a cylindrical coil in which the inner diameter was 200 mm, the outer diameter was 400 mm, and the height was 200 mm. We assumed that 1800 single one-turn coils were arranged at regular intervals in the cylindrical coil: 60 turns in the axial direction and 30 turns in the radial direction. The magnetic field around a single one-turn coil was calculated by using the Biot-Savart law. The magnetic field in the bore was calculated by the superposition of the magnetic fields that were independently formed by the 1800 single one-turn coils.

Figure 12 represents the nondimensionalized magnetic body force vectors $\vec{F}_m = (F_{mR}, F_{m\theta}, F_{mZ})$ in the vessel

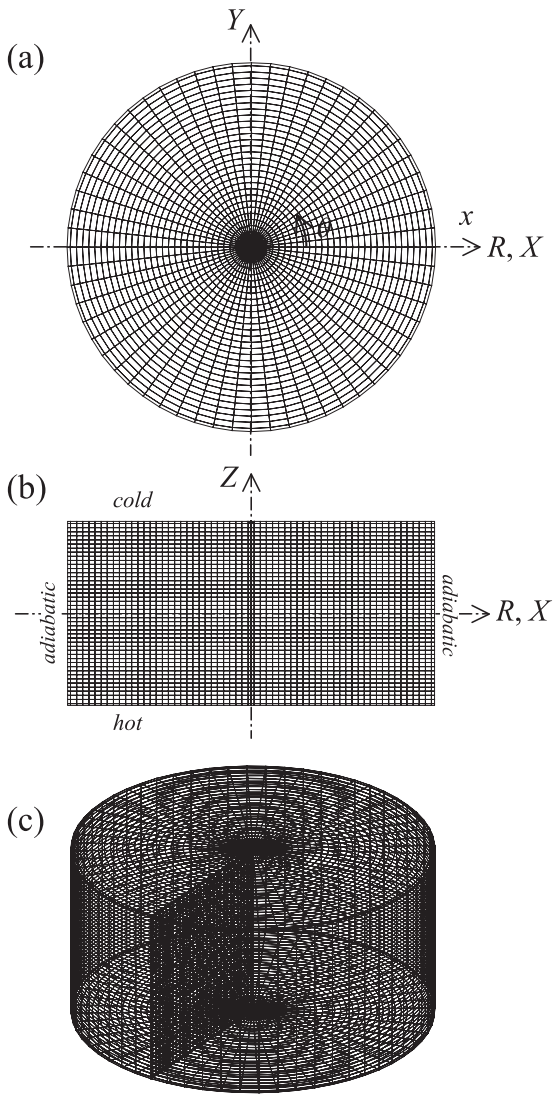

FIG. 10. The computational grid. The grid numbers for the radial (NR), circumferential (NTH), and axial (NZ) directions are 31, 61, and 46, respectively. (a) The cross-sectional views of the grid at the $Z = 0$ plane, (b) the cross-sectional views of the grid at the $Y = 0$ plane, and (c) the crane shot of the grids.

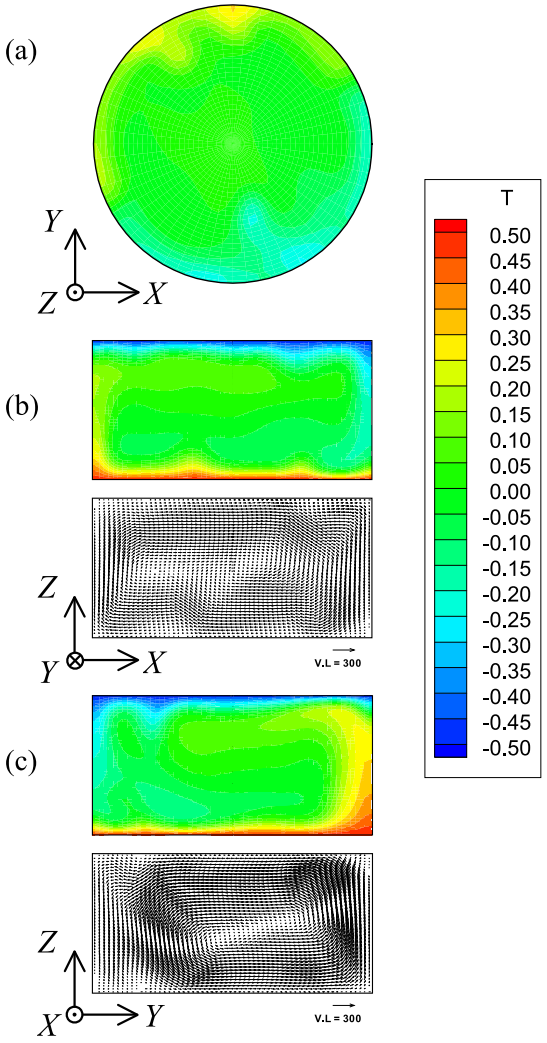

FIG. 11. The computational result of Rayleigh-Benard convection. Pr and Ra are 5.17 and 1.53×10^5, respectively. (a) The horizontal cross-sectional isothermal distribution at the $Z = 0$ plane. The hot solution rises where the distribution is in red or yellow, and the cold solution falls where it is in blue. (b) and (c) show the vertical cross-sectional isothermal and velocity distributions at the $Y = 0$ plane and $X = 0$ plane, respectively.

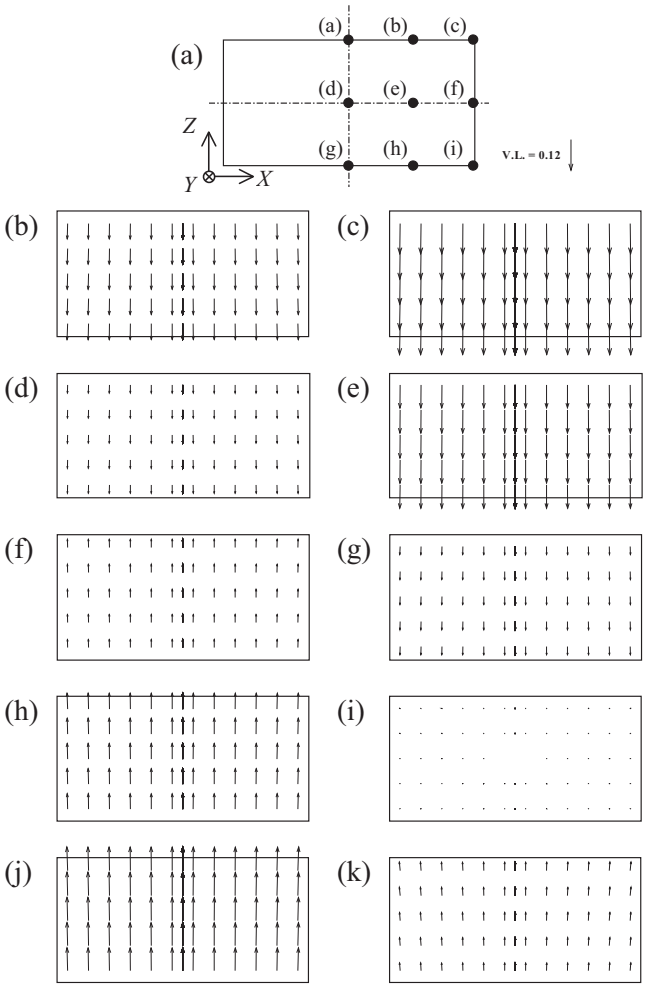

FIG. 12. The nondimensionalized magnetic body force vectors in the vessel located at $Z_{\rm coil} = \pm10h_z$. Only a few arrows in the vessel were selected for the sake of being understandable. (a) shows the representative points (a)–(i) on and in the vessel. The force components of F_{mR}, F_{mZ}, and $F_{mZ} + 1$ on the points (a)–(i) are represented in Appendix B. (b), (d), (f), (h), and (j) show the distribution of the magnetic body force vectors. (c), (e), (g), (i), and (k) show the distribution of driving body force vectors between the gravity and the magnetic body force. (b) and (c) are the cases of $\gamma = 9.76989\times10^{-4}$ at $Z_{\rm coil} = +10h_z$. (d) and (e) are the cases of $\gamma = 4.88494\times10^{-4}$ at $Z_{\rm coil} = +10h_z$. (f) and (g) are the cases of $\gamma = 4.88494\times10^{-4}$ at $Z_{\rm coil} = -10h_z$. (h) and (i) are the cases of $\gamma = 9.76989\times10^{-4}$ at $Z_{\rm coil} = -10h_z$. (j) and (k) are the cases of $\gamma = 1.46548\times10^{-3}$ at $Z_{\rm coil} = -10h_z$. (c) and (e) are the hypergravitational conditions of 2.0 and 1.5 times the gravity downward, respectively. (g) is the partial gravitational condition (0.5 times the gravity downward). (i) is the quasiweightless condition. (k) is the enforced-weightless condition (0.5 times the gravity upward).

located at $Z_{\rm coil} = \pm10h_z$. $Z_{\rm coil}$ is the nondimensionalized cylindrical coordinate system, the origin of which is defined at the magnet center. The h_z is the standard length between the top and the bottom surfaces, and becomes 1.0 in the nondimensionalized system. The results of $\vec{F}_m$ were utilized in the numerical computations, but fewer arrows were selected for the sake of understanding in Fig. 12. The details of Fig. 12 are commented on in Appendix B. Figure 12 shows that the effect of F_{mR} was insignificant in comparison to that of F_{mZ}. This suggests that control over the convection is possible by means of the effect of F_{mZ} only.

In the computations, we calculated the conditions in which F_{mZ} was enhanced downward in Fig. 12(k). We will present in a later section why such enhanced conditions become necessary.

F. Magnetothermal convection under the hypergravitational condition

Figure 13(a) shows the isothermal contours and velocity vectors under the hypergravitational condition. Pr, Ra, and γ are 5.17, 1.53×10^5, and 9.76989×10^{-4}, respectively. The

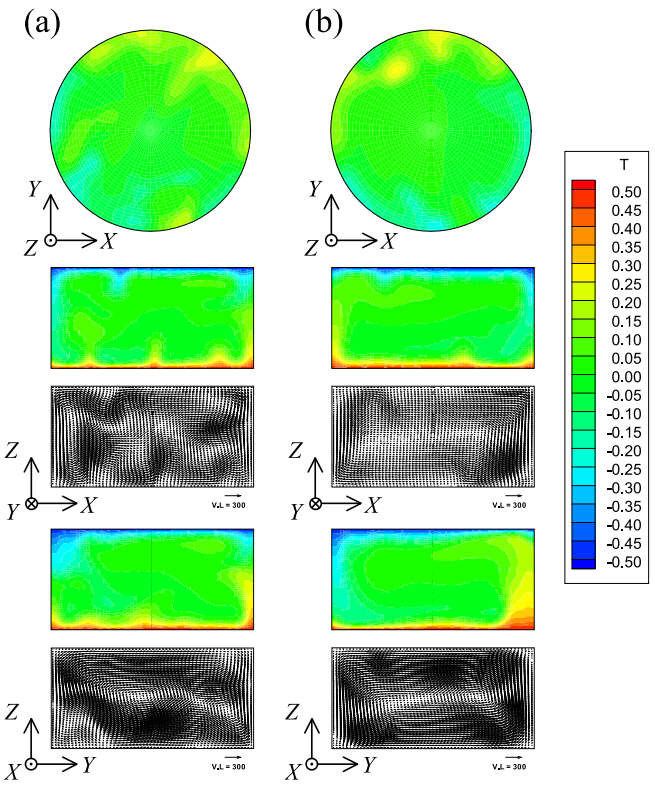

FIG. 13. Numerical isothermal contours and velocity vectors of magnetothermal convection under the hypergravitational condition at $Z_{\rm coil} = +10h_z$. Pr and Ra are 5.17 and 1.53×10^5, respectively. γ are (a) 9.76989×10^{-4} and (b) 4.88494×10^{-4}. The driving body forces of (a) and (b) correspond to the conditions of 2.0 and 1.5 times the gravity downward at the vessel center, respectively.

driving body force vector was 2.0 downward at $Z_{\rm coil} = +10h_z$. Note that the nondimensionalized magnitude of 2.0 corresponds to the condition with two times the gravity. Similarly, Fig. 13(b) shows the hypergravitational cases when Pr, Ra, and γ were 5.17, 1.53×10^5, and 4.88494×10^{-4}, respectively. The driving body force vector was 1.5 downward at $Z_{\rm coil} = +10h_z$. When h_z and α were 10.0 mm and 1.489×10^{-7} m^2/s, respectively, and the temperature was 305.5 K, the actual averaged velocity components u, v, and w and Nu were as presented in Table IV.

In both cases, the convective flows did not change into stable ones. These flows are common phenomena in such a large-scale Ra. The Nu increased slightly more than in the case of Rayleigh-Benard convection. This indicates that the heat transfer on convection was enhanced only a little.

G. Magnetothermal convection under the partial gravitational condition

Figures 14(a) and 14(b) show the results of the isothermal contours and velocity vectors under the partial gravitational condition at $Z_{\rm coil} = -10h_z$. The Pr and Ra were fixed at 5.17 and 1.53×10^5, respectively. The γ in Figs. 14(a) and 14(b) were 4.88494×10^{-4} and 9.28140×10^{-4}, respectively, which corresponds to the conditions in which the nondimensionalized driving body force vector was 0.5 and 0.05 downward, respectively. Figure 14(c) is the case under the quasiweightless condition, and γ was 9.76989×10^{-4}. The actual average velocity components and the Nu are summarized in Table IV.

The convective flows in Fig. 14(a) were unstable. The flows in Figs. 14(b) and 14(c) transitioned to stable axisymmetric ones. No horizontal contours were confirmed at all. These results indicate that a thermal conductive state could not be realized simply by the weightlessness at the vessel center alone.

H. Magnetothermal convection under the enforced-weightless condition

We enhanced the magnetic body force so as to realize the horizontal isothermal contours numerically. We shall designate such condition as "enforced weightlessness." The Pr and Ra were fixed to 5.17 and 1.53×10^5, respectively, and the γ of Figs. 14(d)–14(f) were 1.17239×10^{-3}, 1.36779×10^{-3}, and 1.46548×10^{-3}, respectively, which correspond to the cases of $F_{mZ} = -0.2$, -0.4, and -0.5 at the vessel center, respectively. Figure 12(k) shows the case of $F_{mZ} = -0.5$. When $F_{mZ} = -0.2$, the isothermal contours were barely horizontal. When F_{mZ} was strengthened to over -0.4, the contours settled down horizontally and the difference in appearance was almost equal to the case of -0.5 [see Figs. 14(e) and 14(f)]. By means of these results, the horizontal illuminant observed in the experiment could be realized under the enforced-weightless condition. In the next section, we will determine the critical magnetic flux density and evaluate the heat transfer of magnetothermal convection.

V. DISCUSSION

A. The critical magnetic flux density

The critical magnetic flux density from the convective to the conductive is an essential value to evaluate the heat transfer of magnetothermal convection. In a previous study [14], we used a shallow vessel (actual vessel height was 5 mm) and Ra was set in the range of 7000 and more. It was easily verified by the control over small temperature differences. In the present study, however, we utilized a "moderate" vessel with the aspect ratio of 2.17. We had to increase $\Delta\Theta$ more than 10 K to illuminate the TLC. As a consequence, we were forced to carry out the measurement with quite a large-scale Ra $= 1.53\times10^5$. In the moderate vessel, it is difficult to completely cancel the effect of gravity by F_{mZ}. The ununiformity of magnetic body force in the vessel causes a driving body force on convection.

By using the data in Appendix B, when the F_{mZ} is -1.000 at the vessel center [= the point (d) in Fig. 12(a)] and the vessel location $Z_{\rm coil} = -10h_z$ and g $= 9.76989\times10^{-4}$, the magnitudes of F_{mZ} at the points (a) and (g) in Fig. 12(a) vary to -1.017 and -0.9764, respectively. The Ra at points (a) and (g) is calculated as Ra $= 1.53\times10^5\times|1.017 - 1.000| = 2601$ and Ra $= 1.53\times10^5\times|0.9764 - 1.000| = 3611$, respectively. By theoretical analysis, the Rayleigh-Benard convection is completely suppressed and a thermal conductive state (Nu $=$ 1.0) is realized in the range of Ra < 1707.8 [31]. That is, an enforced-weightless condition is inevitable to realize the conductive state in the moderate vessel.

TABLE IV. Numerical results of heat transfer. Pr = 5.17, Ra = 1.53×10^5, C = 11.5, NR = 31, NTH = 61, NZ = 46.

$Z_{\rm coil}$	γ[a]	$F_{mZ}+1$[d]	Ave. $U\pm$SD (mm/s)[e]	Ave. $V\pm$SD (mm/s)[e]	Ave. $W\pm$SD (mm/s)[e]	Nu $\pm$ SD	Flow
RB	0[b]	1.0	41.57 ± 3.06 (0.62 ± 0.05)	47.33 ± 3.93 (0.71 ± 0.06)	46.73 ± 2.56 (0.70 ± 0.04)	4.71 ± 0.19	unsteady
	9.76989×10^{-4}[c]	2.0	56.58 ± 5.06 (0.84 ± 0.08)	69.87 ± 4.98 (1.04 ± 0.07)	73.96 ± 4.38 (1.10 ± 0.07)	6.10 ± 0.27	unsteady
MC $+10h_z$	4.88494×10^{-4}[c]	1.5	50.36 ± 4.48 (0.75 ± 0.07)	59.40 ± 5.19 (0.89 ± 0.08)	60.73 ± 3.23 (0.90 ± 0.05)	5.45 ± 0.21	unsteady
	4.88494×10^{-4}[c]	0.5	29.76 ± 1.18 (0.44 ± 0.02)	32.13 ± 2.37 (0.48 ± 0.04)	28.93 ± 1.20 (0.43 ± 0.02)	3.61 ± 0.13	unsteady
	9.28140×10^{-4}	0.05	9.49 (0.14)	2.71×10^{-5} (0.00)	11.30 (0.17)	2.31	steady
	9.76989×10^{-4}	0	3.15 (0.047)	5.25×10^{-7} (0.00)	3.72 (0.055)	1.39	steady
MC $-10h_z$	1.17239×10^{-3}	-0.2	0.46 (0.007)	4.41×10^{-7} (0.00)	0.54 (0.008)	1.010	steady
	1.27009×10^{-3}	-0.3	0.39 (0.006)	3.20×10^{-6} (0.00)	0.43 (0.006)	1.006	steady
	1.36779×10^{-3}	-0.4	0.36 (0.005)	3.36×10^{-6} (0.00)	0.37 (0.006)	1.004	steady
	1.46548×10^{-3}	-0.5	0.34 (0.005)	1.53×10^{-6} (0.00)	0.33 (0.005)	1.003	steady

[a]Since we assumed that 1800 single one-turn coils were arranged at regular intervals in the cylindrical coil, more than six significant digits of γ were required.
[b]Averaged value and its SD were calculated by using the data in the range of $0.3<\tau<3.0$.
[c]Averaged value and its SD were calculated by using the data in the range of $0.3<\tau<1.1$.
[d]$F_{mZ}+1$ is the nondimensionalized value at the vessel center [point (d) in Fig. 12(a)].
[e]The values in the parentheses mean the actual velocity (mm/s) calculated by assuming that h_z and α were 10.0 mm and 1.489×10^{-7} m^2/s, respectively, and the temperature was 305.5 K.

In a paramagnetic liquid, the effect of temperature on the susceptibility cannot be ignored by Curie's law. As shown in Fig. 8, $\Delta\Theta$ was 14.70 K at most, and the susceptibility would be changed by 4.8% or less. The magnetic body force would be enhanced by 2.4% more in the vicinity of the top surface (cold) than at the vessel center. Owing to this effect, the magnetic flux density should be enhanced by the magnitude of 1.2% (that is, $\sqrt{1.024}=1.012$).

According to the image in Fig. 7(d), the critical magnetic flux density was 2.85 T. Numerically, the horizontal isothermal contours were barely realized in the case of $F_{mZ}=-0.2$ [see Figs. 14(d)]. Therefore, the critical magnetic flux density at the vessel center is estimated as $b_z=2.85/\sqrt{1+0.2-0.024}=2.63$ T. We will use this value to calculate the magnetic Rayleigh number in the next section.

B. Data analysis with the magnetic Rayleigh number

All the results (experimental and numerical) were summarized by using the critical magnetic flux density of 2.63 T. In Fig. 15(a), the data were plotted on the double-logarithm chart of Ra and Nu. The experimental data are represented by the opened makers, and the numerical data are represented by the filled markers. The Silveston experimental curve [31] was also employed in this figure, the curve of which is determined by the experimental data of heat transfer on Rayleigh-Benard convection with various kinds of fluids (liquid and gas).

As shown in Fig. 15(a), Rayleigh-Benard convection in this study (the symbol is circles) was distributed in the vicinity of the Silveston curve. This suggests that our data agreed well with previous research results [32,33]. In the presence of the downward magnetic body force, the symbol of Nu (reversed triangles) shifted upward on the Silveston curve in relation to the increase in the magnetic body force. Those shifts reflect that the hypergravitational condition enhanced the heat transfer. In the presence of the upward magnetic body force, the symbol of Nu (triangles) shifted downward and went close to 1.0. That is, the heat transfer on convection was weakened as the condition changed from partial gravity to quasiweightlessness and finally completed the thermal conductive state.

Next, all the results were arranged with the magnetic Rayleigh number ($\mathrm{Ra_m}$). The relationship between $\mathrm{Ra_m}$ and Nu is arranged in Fig. 15(b). Practically, $\mathrm{Ra_m}$ is defined by the following correlation:

$$\mathrm{Ra}_m=\mathrm{Ra}\left(1-\gamma\frac{C}{2}\frac{\partial B^2}{\partial Z}\right). \tag{16}$$

As shown in Fig. 15(b), the data of magnetothermal convection were distributed quite well on the Silveston curve. Notice that even if the critical value was regarded as equal to 2.85 T, the relationship distributed closely in the vicinity of the curve (data not shown). The accordance with the Silveston curve

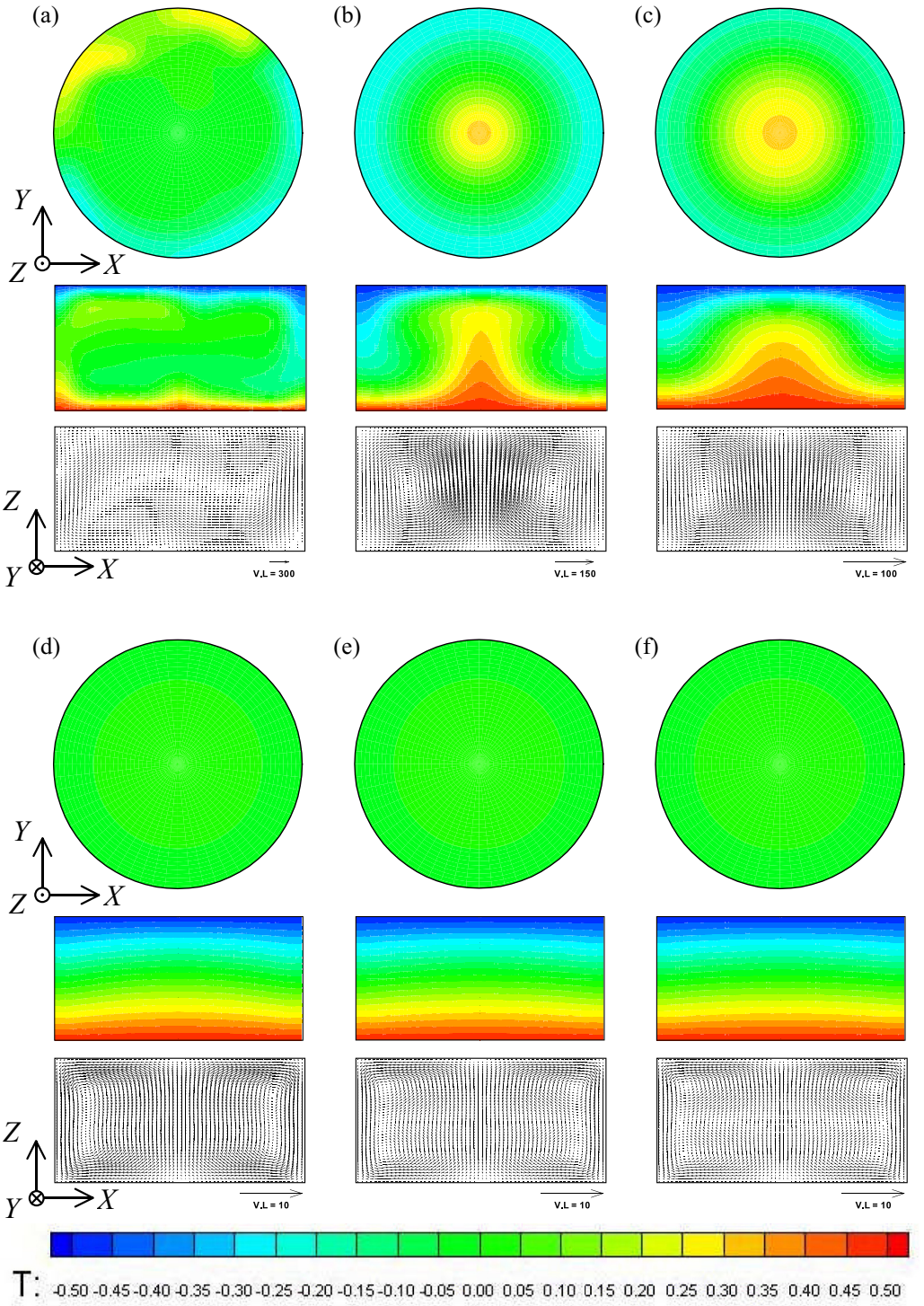

FIG. 14. Numerical isothermal contours and velocity vectors of magnetothermal convection at $Z_{\mathrm{coil}} = -10h_z$. Pr and Ra are 5.17 and 1.53×10^5, respectively. γ are (a) 4.88494×10^{-4}, (b) 9.28140×10^{-4}, (c) 9.76989×10^{-4}, (d) 1.17239×10^{-3}, (e) 1.36779×10^{-3}, and (f) 1.46548×10^{-3}. (a) and (b) are under the partial gravitational condition, the driving body forces of which correspond to the condition of 0.5 and 0.05 times the gravity downward, respectively. (c) is under the quasiweightless condition. (d), (e), and (f) are under the "enforced-weightless" condition, the driving body forces of which correspond to the condition of 0.2, 0.4, and 0.5 times the gravity upward, respectively.

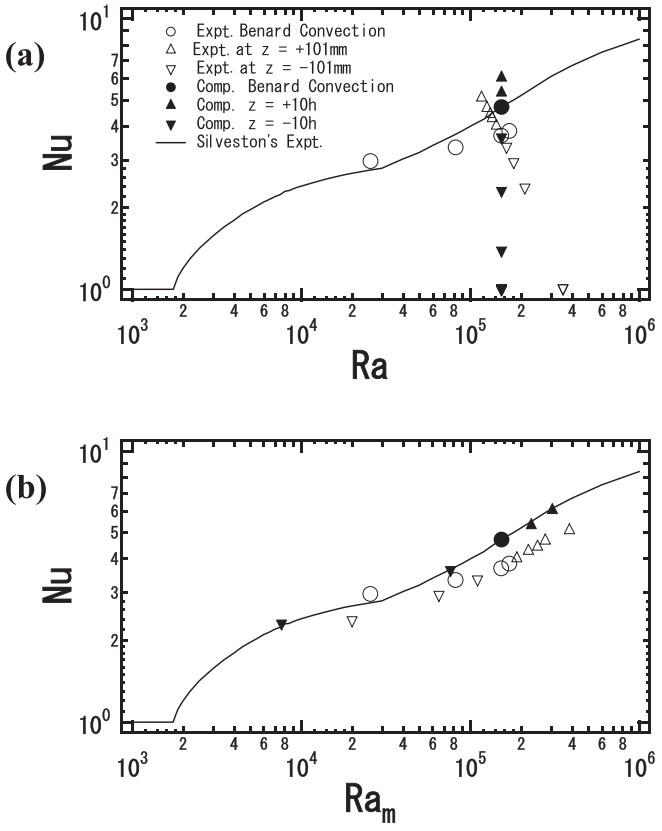

FIG. 15. All the results arranged on double-logarithm charts. (a) The relationship between Ra and Nu, and (b) the relationship between Ra_m and Nu. The Silveston experimental curve is also exhibited in this figure. The experimental results are plotted with the open markers, and the numerical results with the filled markers. The circles show the Rayleigh-Benard convection. The reversed triangles show the hypergravitational condition. The triangles show the partial gravitational condition. We can see that all the data are distributed in the vicinity of the Silveston curve and the heat transfer of magnetothermal convection is arranged on the Silveston curve with Ra_m. In the calculation of Ra_m, the critical magnetic flux density to realize the quasiweightless condition was estimated as 2.63 T.

reveals that the heat transfer of magnetothermal convection can be controlled by Ra_m.

In this study, the experimental data of Nu had a slightly smaller value than those of the Silveston curve. The Silveston curve was provided by the use of a large aspect ratio vessel, whereas our results were brought about with the moderate vessel. The underestimation of Nu may be attributable to resistance from the vessel sidewall.

C. Magnetic effect on the TLC particulates

We used the TLC particulates as a tracer to visualize the convective flows. When the solution is under the quasiweightless condition, the downward driving body force at two times that of gravity acts on the TLC particulates by the magneto-Archimedes effect. This idea may be sufficient to explain the reason why the horizontal illuminant was first visualized near the vessel bottom prior to the vessel top. However, taking a closer look at the sequence figures in Fig. 6, we notice that the particulates have stopped suspending in the illuminant. That is, the TLC particulates were little influenced by the magnetic body force. Since the horizontal illuminant is broken easily, even in the presence of weak flows, they may explain the process in Fig. 6. In the next section, we numerically analyze the flow regimes in the vessel to support this idea.

D. Detail flow regimes in the vessel

By the nondimensionalization techniques [27], the isothermal contour of the thermal Peclet (Pe) number was computed to visualize the flow regimes and their structure. The Pe is defined as the product of the Pr and the Reynolds number (Re), and is transformed as

$$\mathrm{Pe} = \mathrm{Pr} \times \mathrm{Re} = \frac{\nu}{\alpha}\frac{h_z\,|\vec{u}|}{\nu} = \frac{h_z}{\alpha}\sqrt{u^2+v^2+w^2}$$
$$= \sqrt{U^2+V^2+W^2}. \tag{17}$$

The magnetic conditions of γ were varied so as to correspond to the cases of Figs. 11, 13, and 14. All the contours are presented in Fig. 16. The brighter these contours are in the vessel, the stronger the convective flows are. Figure 16(a) shows the Rayleigh-Benard convection ($\gamma = 0$). Figures 16(b) and 16(c) are the cases under the hypergravitational condition. Figures 16(d) and 16(e) are the cases under the partial gravitational condition. Figure 16(f) shows the quasiweightless condition. Figures 16(g)–16(i) are the cases under the enforced-weightless condition. The magnitudes of γ were 0 [Fig. 16(a)], 9.76989×10^{-4} [Figs. 16(b) and 16(f)], 4.88494×10^{-4} [Figs. 16(c) and 16(d)], 9.28140×10^{-4} [Fig. 16(e)], 1.17239×10^{-3} [Fig. 16(g)], 1.36779×10^{-3} [Fig. 16(h)], and 1.46548×10^{-3} [Fig. 16(i)].

As shown in Figs. 16(a)–16(d), the convective flows were unstable. They may have been turbulent since Pe was so large in most parts of the vessel. Figures 16(e)–16(i) show that the flows became axisymmetric. In particular, the regimes in flows in Figs. 16(e) and 16(f) were similar to each other and strong flows were induced around the vessel center. On the other hand, in the flows in Figs. 16(g)–16(i), hardly any flows occurred around the vessel center (colored in blue). The flows were induced in the vicinity of the vessel wall (colored in yellow or red). These results support that the stagnated region around the vessel center ($\mathrm{Pe} < 0.6$) was suitable for illuminating the TLC.

There have been many reports on flow structures in a conventional Rayleigh-Benard convection [34–37], but to analyze the structures in magnetothermal convection we have to consider the influence of the radial component of the magnetic body force [38–40]. This influence is determined by the magnitude of $(\vec{b}\cdot\vec{\nabla})\vec{b}$, which, in most cases, depends on the location of the vessel in the magnet bore. It was impossible to investigate the illuminant of TLC in the details of the structure, and this is a limitation of this study. Further study and improvement will be necessary in future research.

VI. CONCLUSIONS

We visualized magnetothermal convection and analyzed the heat transfer by experiments and numerical computations. We developed an original observation system and measurement

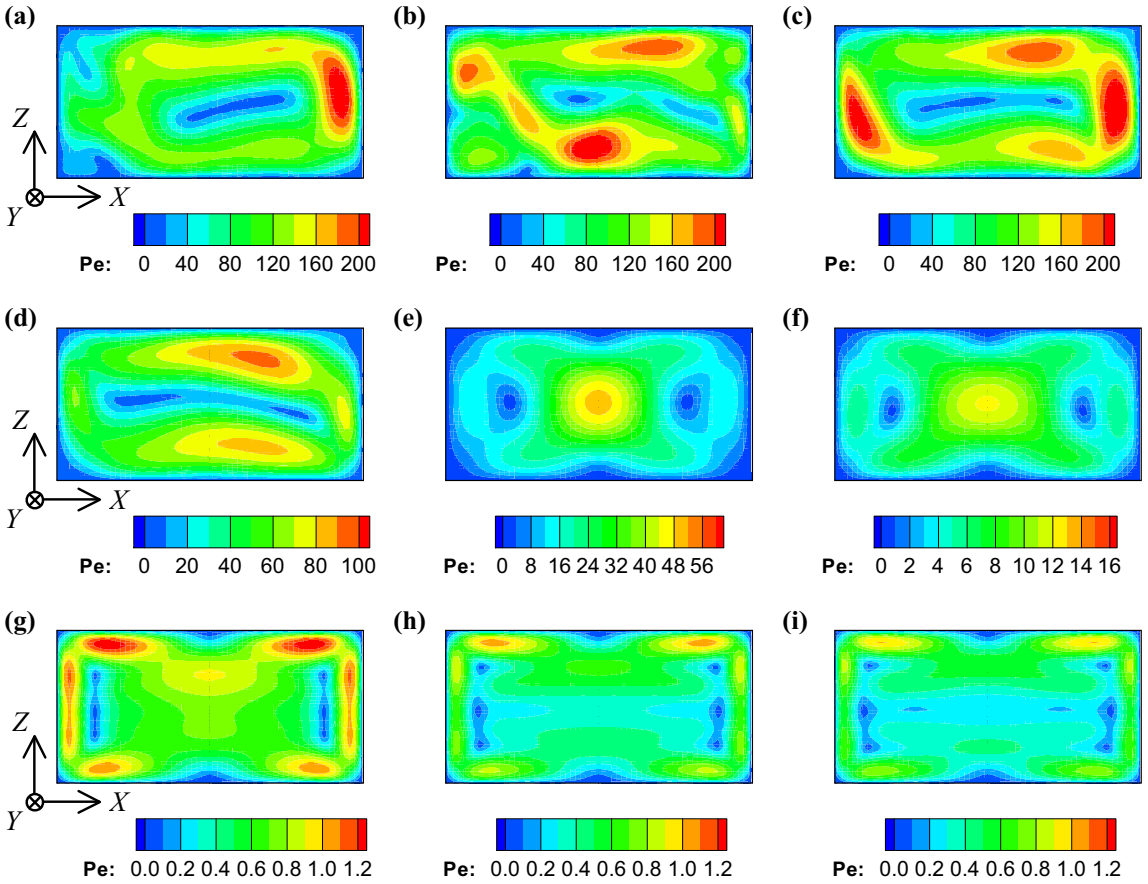

FIG. 16. Numerical isothermal contours of the Pe number. The vessel center position of (b) and (c) is at $Z_{\mathrm{coil}} = +10h_z$, and that of (d)–(i) is at $Z_{\mathrm{coil}} = -10h_z$. γ are (a) 0, (b) and (f) 9.76989×10^{-4}, (c) and (d) 4.88494×10^{-4}, (e) 9.28140×10^{-4}, (g) 1.17239×10^{-3}, (h) 1.36779×10^{-3}, and (i) 1.46548×10^{-3}. (a) is under the Rayleigh-Benard convection. (b) and (c) are under the hypergravitational condition, the driving body forces of which correspond to the conditions of 2.0 and 1.5 times the gravity downward, respectively. (d) and (e) are under the partial gravitational condition, the driving body forces of which correspond to the conditions of 0.5 and 0.05 times the gravity downward, respectively. (f) is under the quasiweightless condition. (g), (h), and (i) are under the enforced-weightless condition, the driving body forces of which correspond to the conditions of 0.2, 0.4, and 0.5 times the gravity upward, respectively.

equipment based on the Rayleigh-Benard model (aspect ratio 2.17) in a solenoidal superconducting magnet to visualize *in situ* from the side view. The working fluid of convection was an aqueous gadolinium nitrate solution (paramagnetic substance), and the isothermal contour of convection was visualized by the addition of a thermochromic liquid crystal (TLC). Under a large upward magnetic body force, we succeeded in visualizing the horizontal isothermal illuminant of the TLC, which reveals the realization of a quasiweightless condition in the Rayleigh-Benard model; that is, we have acheived the visualization of the horizontal illuminant on magnetothermal convection. We also observed the transition process on convection from the conductive state to the inducement of convective flows by upwardly adjusting the magnitude of the magnetic body force. A similar isothermal illuminant could not be visualized under a hypergravitational condition and Rayleigh-Benard convection.

The amount of heat transfer in this system was measured by the method of Churchill and Ozoe, and then the Rayleigh number (Ra) and Nusselt number (Nu) were experimentally determined. We identified quantitatively that the heat transfer on convection was enhanced by the downward magnetic body force and suppressed by the upward magnetic body force, as compared to that in the Rayleigh-Benard convection.

The convective flows in the present model (Prandtl number = 5.17, $\mathrm{Ra} = 1.53\times10^5$, aspect ratio 2.0) were numerically simulated by three-dimensional computation. We introduced the magnetic Rayleigh number $\mathrm{Ra_m}$ instead of Ra, and the experimental and numerical data of Nu were plotted versus the $\mathrm{Ra_m}$. These results coincided well with the Silveston experimental curve with $\mathrm{Ra_m}$, showing that the heat transfer on magnetothermal convection can be measured by the use of $\mathrm{Ra_m}$.

ACKNOWLEDGMENTS

This research was supported by MEXT/JSPS, KAKENHI, Grant No. JP15K04669. We were also supported by the Osaka Ohtani University Research Fund (Pharmaceutical Sciences). This work was carried out at the Center for Advanced High Magnetic Field Science in Osaka University under the Visiting Researcher's Program of the Institute for Solid State Physics,

TABLE V. Thermal properties of water [29,41,42].

	30 °C	40 °C
Density ρ (kg/m^3)	995.7	992.3
Thermal diffusivity α (m^2/s)	1.48×10^{-7}	1.52×10^{-7}
Kinematic viscosity ν (m^2/s)	8.03×10^{-7}	6.68×10^{-7}
Volumetric coefficient of expansion β (1/K)	2.90×10^{-4}	3.80×10^{-4}
Pr	5.41	4.39

the University of Tokyo. The superconducting magnet in this work belongs to Dr. Satoshi Tomita, Quantum Material Science Laboratory, Graduate School of Material Science, Nara Institute of Science and Technology. We would like to express our deepest gratitude for support from all these sources.

APPENDIX A

The thermal properties of water are given in Table V.

When the temperature was 305.5 K, ρ, α, ν, β, and Pr were interpolated as 994.9 kg/m^3, 1.49×10^{-7} m^2/s, 7.71×10^{-7} m^2/s, 3.11×10^{-4} m^2/s, and 5.17 K^{-1}, respectively. Then, the parameter C was calculated as

$$C = 1 + \frac{1}{\beta_0\Theta_0} = 1 + \frac{1}{3.11\times10^{-4}\times305.5} = 11.5.$$

In this study, the vessel height h_z and the temperature difference $\Delta\Theta$ were 9.20×10^{-3} m and 7.378 K, respectively. By using the thermal properties mentioned above, Ra was

$$\begin{aligned}\mathrm{Ra} &= \frac{g\beta\Delta\Theta h_z^3}{\alpha\nu} \\ &= \frac{9.806\times3.11\times10^{-4}\times7.378\times(9.20\times10^{-3})^3}{1.49\times10^{-7}\times7.71\times10^{-7}} \\ &= 1.53\times10^5.\end{aligned}$$

Now, magnetic flux density in the vessel was substituted by the vertical component of b_z. In this study, the b_z was modulated from 3.0 to 2.75 T at $z_{\mathrm{coil}} = 0$. The b_z in the vessel (at $z_{\mathrm{coil}} = \pm101$ mm) corresponds to the range from 2.12 to 1.94 T.

The measurement of electric conductivity of a 0.15 mol/kg $Gd(NO_3)_3$ solution was newly carried out. The electric conductivity σ resulted in 3.7 S/m. As a consequence, the Hartmann number Ha was calculated as follows:

when b_z is 2.12 T :

$$\mathrm{Ha} = b_z\frac{h_z}{2}\sqrt{\frac{\sigma}{\rho\,\nu}} = 2.12\times\frac{9.20\times10^{-3}}{2}\times\sqrt{\frac{3.7}{994.9\times\ 7.71\times10^{-7}}} = 0.68;$$

when b_z is 1.94 T :

$$\mathrm{Ha} = 1.94\ \times\ \frac{9.20\times10^{-3}}{2}\sqrt{\frac{3.7}{994.9\times\ 7.71\times10^{-7}}} = 0.62.$$

APPENDIX B

Table VI summarizes the components of nondimensionalized magnetic body force calculated at representative points. The representative points (a)–(i) on and in the vessel are shown in Fig. 12(a). Point (d) is particularly important. It represents the vessel center, and the driving body force on convection was characterized by this point. Some of the distributions of the magnetic body force are represented in Fig. 12. We can find that the effect of F_{mR} is insignificant in comparison to that of F_{mZ}.

TABLE VI. Components of nondimensionalized magnetic body force calculated at representative points in Fig. 12.

Z_{coil}	γ (G)	$\vec{F}_m$	(a)	(b)	(c)	(d)	(e)	(f)	(g)	(h)	(i)
$+10h_z$	9.76989×10^{-4}	F_{mR}	0.4577×10^{-3}	0.1289×10^{-1}	0.2461×10^{-1}	0.5752×10^{-3}	0.1576×10^{-1}	0.3008×10^{-1}	0.6972×10^{-3}	0.1872×10^{-1}	$0.3572D\times10^{-1}$
	[Figs. 12(b), 12(c)]	F_{mZ}	0.9764	0.9779	0.9818	1.000	1.002	1.006	1.017	1.019	1.023
		$F_{mZ}+1$	1.976	1.978	1.982	2.000	2.002	2.006	2.017	2.019	2.023
	4.88494×10^{-4}	F_{mR}	0.2289×10^{-3}	0.6446×10^{-2}	0.1230×10^{-1}	0.2876×10^{-3}	0.7879×10^{-2}	0.1504×10^{-1}	0.3486×10^{-3}	0.9358×10^{-2}	0.1786×10^{-1}
	[Figs. 12(d), 12(e)]	F_{mZ}	0.4882	0.4889	0.4909	0.5001	0.5008	0.5029	0.5086	0.5094	0.5114
		$F_{mZ}+1$	1.488	1.489	1.491	1.500	1.501	1.503	1.509	1.509	1.511
	4.88494×10^{-4}	F_{mR}	0.3486×10^{-3}	0.9358×10^{-2}	0.1786×10^{-1}	0.2876×10^{-3}	0.7879×10^{-2}	0.1504×10^{-1}	0.2289×10^{-3}	0.6446×10^{-2}	0.1230×10^{-1}
	[Figs. 12(f), 12(g)]	F_{mZ}	–0.5086	–0.5094	–0.5114	–0.5001	–0.5008	–0.5029	–0.4882	–0.4889	–0.4909
		$F_{mZ}+1$	0.4914	0.4906	0.4886	0.4999	0.4992	0.4971	0.5118	0.5111	0.5091
	9.28140×10^{-4}	F_{mR}	0.6624×10^{-3}	0.1778×10^{-1}	0.3394×10^{-1}	0.5464×10^{-3}	0.1497×10^{-1}	0.2857×10^{-1}	0.4348×10^{-3}	0.1225×10^{-1}	0.2338×10^{-1}
		F_{mZ}	–0.9663	–0.9678	–0.9717	–0.9501	–0.9516	–0.9555	–0.9276	–0.9290	–0.9327
		$F_{mZ}+1$	0.3372×10^{-1}	0.3223×10^{-1}	0.2828×10^{-1}	0.4987×10^{-1}	0.4841×10^{-1}	0.4454×10^{-1}	0.7242×10^{-1}	0.7102×10^{-1}	0.6732×10^{-1}
	9.76989×10^{-4}	F_{mR}	0.6972×10^{-3}	0.1872×10^{-1}	0.3572×10^{-1}	0.5752×10^{-3}	0.1576×10^{-1}	0.3008×10^{-1}	0.4577×10^{-3}	0.1289×10^{-1}	0.2461×10^{-1}
	[Figs. 12(h), 12(i)]	F_{mZ}	–1.017	–1.019	–1.023	–1.000	–1.002	–1.006	–0.9764	–0.9779	–0.9818
		$F_{mZ}+1$	-0.1713×10^{-1}	-0.1871×10^{-1}	-0.2286×10^{-1}	-0.1383×10^{-3}	-0.1678×10^{-2}	-0.5743×10^{-2}	0.2360×10^{-1}	0.2212×10^{-1}	0.1823×10^{-1}
$-10h_z$											
	1.17239×10^{-3}	F_{mR}	0.8367×10^{-3}	0.2246×10^{-1}	0.4287×10^{-1}	0.6902×10^{-3}	0.1891×10^{-1}	0.3609×10^{-1}	0.5493×10^{-3}	0.1547×10^{-1}	0.2953×10^{-1}
		F_{mZ}	–1.221	–1.222	–1.227	–1.200	–1.202	–1.207	–1.172	–1.173	–1.178
		$F_{mZ}+1$	–0.2206	–0.2225	–0.2274	–0.2002	–0.2020	–0.2069	–0.1717	–0.1735	–0.1781
	1.36779×10^{-3}	F_{mR}	0.9761×10^{-3}	0.2620×10^{-1}	0.5001×10^{-1}	0.8053×10^{-3}	0.2206×10^{-1}	0.4211×10^{-1}	0.6408×10^{-3}	0.1805×10^{-1}	0.3445×10^{-1}
		F_{mZ}	–1.424	–1.426	–1.432	–1.400	–1.402	–1.408	–1.367	–1.369	–1.374
		$F_{mZ}+1$	–0.4240	–0.4262	–0.4320	–0.4002	–0.4024	–0.4080	–0.3670	–0.3690	–0.3745
	1.46548×10^{-3}	F_{mR}	0.1046×10^{-2}	0.2807×10^{-1}	0.5358×10^{-1}	0.8628×10^{-3}	0.2364×10^{-1}	0.4511×10^{-1}	0.6866×10^{-3}	0.1934×10^{-1}	0.3691×10^{-1}
	[Figs. 12(j), 12(k)]	F_{mZ}	–1.526	–1.528	–1.534	–1.500	–1.503	–1.509	–1.465	–1.467	–1.473
		$F_{mZ}+1$	–0.5257	–0.5281	–0.5343	–0.5002	–0.5025	–0.5086	–0.4646	–0.4668	–0.4726

[1] M. Faraday, Philos. Mag. **31**(210), 401 (1847).

[2] L. D. Landau and E. M. Lifshits, in *Course of Theoretical Physics, Vol. 8, Electrodynamics of Continuous Media* (Pergamon Press, Oxford, 1960), p. 142.

[3] E. Beaugnon and R. Tournier, Nature (London) **349**, 470 (1991).

[4] D. Braithwaite, E. Beaugnon, and R. Tournier, Nature (London) **354**, 134 (1991).

[5] N. I. Wakayama, Combust. Flame **93**, 207 (1993).

[6] H. Uetake, J. Nakagawa, N. Hirota, and K. Kitazawa, J. Appl. Phys. **85**, 5735 (1999).

[7] S. X. Lin, M. Zhou, A. Azzi, G. J. Xu, N. I. Wakayama, and M. Ataka, Biochem. Biophys. Res. Commun. **275**, 274 (2000).

[8] P. W. G. Poodt, M. C. R. Heijna, P. C. M. Christianen, W. J. P. van Enckevort, W. J. de Grip, K. Tsukamoto, J. C. Maan, and E. Vlieg, Cryst. Growth Des. **6**, 2275 (2006).

[9] T. Tagawa, R. Shigemitsu, and H. Ozoe, Int. J. Heat Mass Transfer **45**, 267 (2002).

[10] S. Maki, T. Tagawa, and H. Ozoe, J. Heat Transfer ASME **124**, 667 (2002).

[11] M. Kaneda, T. Tagawa, and H. Ozoe, J. Heat Transfer ASME **124**, 17 (2002).

[12] H. Nakamura, T. Takayama, H. Uetake, N. Hirota, and K. Kitazawa, Phys. Rev. Lett. **94**, 144501 (2005).

[13] I. Mogi, C. Umeki, K. Takahashi, S. Awaji, K. Watanabe, and M. Motokawa, Jpn. J. Appl. Phys. **42**, L715 (2003).

[14] S. Maki, M. Ataka, T. Tagawa, H. Ozoe, and W. Mori, AIChE J. **51**, 1096 (2005).

[15] P. Filar, E. Fornalik, T. Tagawa, H. Ozoe, and J. S. Szmyd, J. Heat Transfer ASME **128**, 183 (2006).

[16] T. H. Solomon and J. P. Gollub, Phys. Rev. Lett. **64**, 2382 (1990).

[17] T. A. Kowalewski, *Proceedings of the 2001 International Symposium on Environmental Hydraulics* (ISEH, Chicago, Illinois, 2001).

[18] T. A. Kowalewski, *Proceedings of the 4th International Symposium on Particle Image Velocimetry* (Institute of Aerodynamics and Flow Technology, Göttingen, Germany, 2001).

[19] J. A. Stasiek and T. A. Kowalewski, Opto-Electron. Rev. **10**, 1 (2002).

[20] M. Ciofalo, M. Signorino, and M. Simiano, Exp. Fluids **34**, 156 (2003).

[21] T. P. Bednarz, C. Lei, and J. C. Patterson, in *Proceedings of the Sixteenth Australasian Fluid Mechanics Conference, Gold Coast, Australia* (The University of Queensland, Brisbane, 2007), p. 1165.

[22] K. U. Kobayashi, N. Oikawa, and R. Kurita, Sci. Rep. **5**, 18667 (2015).

[23] See Supplemental Material at http://link.aps.org/supplemental/10.1103/PhysRevE.98.033109 for short movies of the magnetothermal convection in this study.

[24] H. Ozoe and S. W. Churchill, AIChE Symp. Ser. **69**, 126 (1973).

[25] J. P. Holman, in *Heat Transfer*, 7th ed. (McGraw-Hill, London, 1992), p. 2.

[26] *CRC Handbook of Chemistry and Physics*, 67th ed. (CRC Press, Boca Raton, FL, 1986–1987).

[27] J. D. Hellums and S. W. Churchill, AIChE J. **10**, 110 (1964).

[28] M. Akamatsu, M. Higano, Y. Takahashi, and H. Ozoe, Numer. Heat Transfer, Part A **43**, 9 (2003).

[29] K. Nishikawa and Y. Fujita, in *Heat Transfer*, 12th ed. (Rikogakusha, Tokyo, 1992), p. 457 (in Japanese).

[30] C. W. Hirt, B. D. Nichols, and N. C. Romero, Los Alamos Scientific Laboratory, LA-5852, 1975.

[31] C. Chandrasekhar, in *Hydrodynamic and Hydromagnetic Stability* (Oxford University Press, New York, 1961), p. 68.

[32] H. Frick, F. H. Busse, and R. M. Clever, J. Fluid Mech. **127**, 141 (1983).

[33] R. M. Clever and F. H. Busse, J. Fluid Mech. **271**, 103 (1994).

[34] D. Funfschilling, E. Brown, A. Nikolaenko, and G. Ahlers, J. Fluid Mech. **536**, 145 (2005).

[35] H. Yang and Z. Zhu, Int. Commun. Heat Mass Transf. **33**, 184 (2006).

[36] J. Bailon-Cuba, M. S. Emran, and J. Schumacher, J. Fluid Mech. **655**, 152 (2010).

[37] P. J. Sakievich, Y. T. Peet, and R. J. Adrian, Int. J. Heat Fluid Flow **61**, 183 (2016).

[38] S. Maki and M. Ataka, Jpn. J. Appl. Phys. **44**, 1132 (2005).

[39] S. Maki and N. Hirota, J. Food Eng. **120**, 31 (2014).

[40] S. Maki, K. Tanaka, and S. Morimoto, J. Phys. Soc. Jpn. **86**, 024402 (2017).

[41] J. P. Holman, in *Heat Transfer*, 7th ed. (McGraw-Hill, London, 1992), p. 663.

[42] *Rika Nenpyo (Chronological Scientific Tables)*, edited by National Astronomical Observatory (Maruzen, Tokyo, 1997), p. 539 (in Japanese).